INTERNATIONAL JOURNAL FOR NUMERICAL METHODS IN ENGINEERING
Int. J. Numer. Meth. Engng 2002; **53**:1903–1935 (DOI: 10.1002/nme.364)

Finite element evaluation of mixed mode stress intensity factors in functionally graded materials

Jeong-Ho Kim and Glaucio H. Paulino*,†

Department of Civil and Environmental Engineering, University of Illinois at Urbana-Champaign, Newmark Laboratory, 205 North Mathews Avenue, Urbana, IL 61801, U.S.A.

SUMMARY

This paper is directed towards finite element computation of fracture parameters in functionally graded material (FGM) assemblages of arbitrary geometry with stationary cracks. Graded finite elements are developed where the elastic moduli are smooth functions of spatial co-ordinates which are integrated into the element stiffness matrix. In particular, stress intensity factors for mode I and mixed-mode two-dimensional problems are evaluated and compared through three different approaches tailored for FGMs: path-independent J_k^*-integral, modified crack-closure integral method, and displacement correlation technique. The accuracy of these methods is discussed based on comparison with available theoretical, experimental or numerical solutions. Copyright © 2001 John Wiley & Sons, Ltd.

KEY WORDS: functionally graded material (FGM); stress intensity factor (SIF); J_k^*-integral; modified crack closure; displacement correlation; finite element method (FEM)

1. INTRODUCTION

The emergence of *functionally graded materials*, or FGMs, is the outcome of the need to accommodate material exposure to non-uniform service requirements. Such materials have been the focus of intense investigations, which in Japan and Germany, have become highly coordinated in their technical emphasis and government financial support. The Fourth International Symposium on FGMs was held in Tsukuba City, Japan, in 1996 (FGM'96); and the Fifth International Symposium on FGMs was held in Dresden, Germany, in 1998 (FGM'98). Recently, the Sixth International Symposium on FGMs was held in the United States at Estes Park, Colorado (FGM'2000).

Although the initial emphasis for FGMs focused on the synthesis of thermal barrier coatings for space-type applications [1], subsequent investigations have addressed a wide variety of applications [2–4]. These include the potential use of FGMs in nuclear fusion and fast

*Correspondence to: Glaucio H. Paulino, Department of Civil and Environmental Engineering, University of Illinois at Urbana-Champaign, Newmark Laboratory, 205 North Mathews Avenue, Urbana, IL 61801, U.S.A.
†E-mail: paulino@uiuc.edu

Contract/grant sponsor: NSF; contract/grant number: CMS-9996378

Received 20 November 2000
Revised 16 May 2001

breeder reactors as first-wall composite materials [5]; in electronic and magnetic applications as piezoelectric and thermoelectric devices, and as high density magnetic recording media and position measuring devices [6–9]; in optical applications, e.g. graded refractive index materials in audio-video disks [10]; in thermionic applications, e.g. thermionic converters [11]; in biomaterials, e.g. dental and other implants [12, 13]; and in other applications, e.g. the development of fire retardant doors [14].

FGMs possess the distinguishing feature of non-homogeneity with regard to thermomechanical and strength related properties including yield strength, fracture toughness, fatigue and creep behaviour. Next, a few related papers in the context of finite element modelling of fracture of FGMs are briefly reviewed. Eischen [15] has done an early investigation of mixed-mode cracks in non-homogeneous materials which included three examples that were analysed by the finite element method (FEM). Gu *et al.* [16] have presented a simplified method for calculating the crack-tip field of FGMs using the equivalent domain integral (EDI) technique. Anlas *et al.* [17] have evaluated SIFs in FGMs by the FEM where the material property variation was discretized by assigning different homogeneous elastic properties to each element. Both Gu *et al.* [16] and Anlas *et al.* [17] have considered a Mode I crack where the crack is parallel to the material gradation and have used the FEM code ABAQUS in their analyses. Marur and Tippur [18] have considered a crack normal to the elastic gradient and have performed FEM analysis in conjunction with experiments. Bao and Wang [19] have studied multiple cracking in functionally graded ceramic/metal coatings. Bao and Cai [20] have investigated delamination cracking in a functionally graded ceramic/metal substrate. Lee and Erdogan [21] have calculated residual thermal stresses in FGMs. It is worth mentioning that all the previous models cited in this paragraph are problem specific. *Thus the goal of the present paper is to develop a general purpose FEM formulation and implementation for elastic FGMs and for fracture of FGMs considering mixed-mode cracks*. To this effect, techniques to evaluate mixed-mode SIFs, such as the J_k^*-integral, are specifically tailored for FGMs.

The remainder of this paper, which is devoted to finite element modelling of fracture in FGMs, is organized as follows. The next section briefly reviews crack tip fields. Section 3 addresses the displacement correlation technique (DCT), and Section 4 presents the modified crack closure (MCC) method. Section 5 details the J_k^* $(k = 1, 2)$ formulation accounting for material non-homogeneity. These three methods (DCT, MCC, J_k^*-integral) are presented in the context of mixed-mode fracture in FGMs. Section 6 discusses some relevant aspects of the FEM implementation. To validate all the previous development, Section 7 presents many numerical results which, whenever possible, are compared to available theoretical, experimental, or numerical solutions. Finally, Section 8 concludes the present investigation.

2. CRACK TIP FIELDS IN FGMs

The eigenfunction expansion technique proposed by Williams [22] has been widely used to investigate the nature of the near-tip fields in a cracked body. Eischen [15] has used an extension of this procedure to establish the general form of the stress and displacement fields near a crack tip in a non-homogeneous material where the elastic moduli vary with position $(\mathbf{x})$ such that the Young's modulus $E \equiv E(\mathbf{x})$ and Poisson's ratio $\nu \equiv \nu(\mathbf{x})$ are continuous, bounded, and differentiable functions. This result was further confirmed by Jin and Noda [23] for materials with piecewise differentiable property variations. Figure 1 shows a crack in

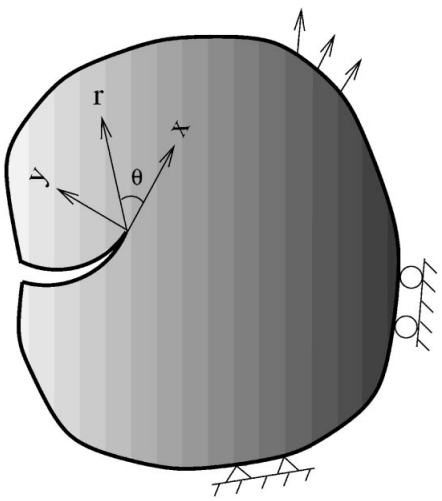

Figure 1. Cartesian (x, y) and polar (r, θ) co-ordinate systems at the crack tip.

a two dimensional FGM elastic body with applied tractions and specified displacements on the boundary resulting in a state of generalized plane stress or plane strain. Local Cartesian and cylindrical co-ordinates are fixed at the crack tip, body forces are neglected, and crack faces are assumed to be traction-free. The following approximate expressions for stresses are obtained [15, 23]:

$$\begin{aligned}
\sigma_{11} &\cong \frac{K_{\mathrm{I}}}{\sqrt{2\pi r}} f_{11}^{\mathrm{I}}(\theta) + \frac{K_{\mathrm{II}}}{\sqrt{2\pi r}} f_{11}^{\mathrm{II}}(\theta) + \sigma_{x0} + \cdots \\
\sigma_{22} &\cong \frac{K_{\mathrm{I}}}{\sqrt{2\pi r}} f_{22}^{\mathrm{I}}(\theta) + \frac{K_{\mathrm{II}}}{\sqrt{2\pi r}} f_{22}^{\mathrm{II}}(\theta) + \cdots \\
\sigma_{12} &\cong \frac{K_{\mathrm{I}}}{\sqrt{2\pi r}} f_{12}^{\mathrm{I}}(\theta) + \frac{K_{\mathrm{II}}}{\sqrt{2\pi r}} f_{12}^{\mathrm{II}}(\theta) + \cdots
\end{aligned} \tag{1}$$

where K_{I} and K_{II} are the modes I and II stress intensity factors (SIFs), respectively. The stress component σ_{x0} is called 'non-singular stress', and it has been associated with crack kinking phenomena. The symbols $f_{ij}^{\mathrm{I}}(\theta)$ and $f_{ij}^{\mathrm{II}}(\theta)$ $(i, j = 1, 2)$ denote the standard angular distribution functions for homogeneous materials and can be found in many references in fracture mechanics, e.g. Eftis *et al.* [24]. Nevertheless, the angular variation of the components of stress which correspond to terms $O(r^{1/2})$ and higher do change due to material non-homogeneity [15].

The present analysis also leads to the near-tip displacement of the form [15, 23]:

$$\begin{aligned}
u_1 &\cong \frac{K_{\mathrm{I}}}{\mu_{\mathrm{tip}}} \sqrt{\frac{r}{2\pi}} g_1^{\mathrm{I}}(\theta) + \frac{K_{\mathrm{II}}}{\mu_{\mathrm{tip}}} \sqrt{\frac{r}{2\pi}} g_1^{\mathrm{II}}(\theta) + \cdots \\
u_2 &\cong \frac{K_{\mathrm{I}}}{\mu_{\mathrm{tip}}} \sqrt{\frac{r}{2\pi}} g_2^{\mathrm{I}}(\theta) + \frac{K_{\mathrm{II}}}{\mu_{\mathrm{tip}}} \sqrt{\frac{r}{2\pi}} g_2^{\mathrm{II}}(\theta) + \cdots
\end{aligned} \tag{2}$$

where μ_{tip} is the shear modulus at the crack tip and the angular functions $g_i^{\text{I}}(\theta)$, $g_i^{\text{II}}(\theta)$ $(i=1,2)$ can be found, for example, in Eftis *et al.* [24]. Again, the nature of the near crack tip displacement field is the same as for homogeneous materials. However, the terms $O(r^{3/2})$ and higher do not exhibit the same spatial dependence as the corresponding terms for a homogeneous material [15].

The SIFs are functions of material gradients, external loading and geometry. The material gradients do not affect the order of singularity and the angular functions of the crack tip fields, but do affect the SIFs. However, this dependence cannot be determined by techniques such as eigenfunction expansion [22, 25]. Methods to accomplish this task will be discussed in the next three sections of this paper (which address the DCT, MCC, and J_k^*-integral, respectively).

3. DISPLACEMENT CORRELATION TECHNIQUE (DCT) FOR FGMs

The DCT is one of the simplest methods to evaluate SIFs. It consists of correlating numerical results for displacement at specific locations on the crack with available analytical solutions. For quarter point singular elements, the crack opening displacement (COD) profile at $x=-r$ is given by [26].

$$\text{COD}(-r)=(4u_{2,i-1}-u_{2,i-2})\sqrt{\frac{r}{\Delta a}} \tag{3}$$

where $u_{2,i-1}$ and $u_{2,i-2}$ are the relative displacements to the crack tip in the x_2 direction at locations $(i-1)$ and $(i-2)$, r is the distance from the crack tip along the x_1 direction, and Δa is a characteristic length associated to the crack tip elements (see Figure 2).

For FGMs, material properties need to be considered at the crack tip location. Thus, consistently with Equation (2), the analytical expression for COD$(-r)$, neglecting higher order

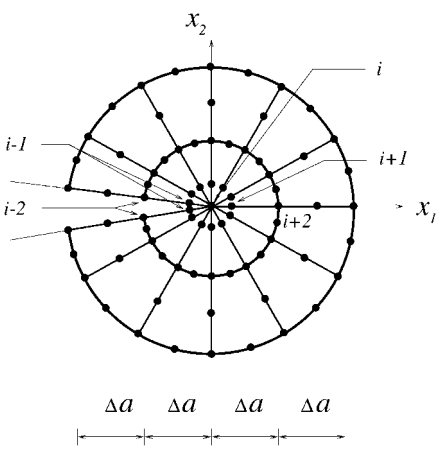

Figure 2. Crack tip rosette of singular quarter-point (1st ring) and regular (2nd ring) finite elements.

terms, can be written as

$$\mathrm{COD}(-r) = K_{\mathrm{I}} \left(\frac{\kappa + 1}{\mu} \right)_{\mathrm{tip}} \sqrt{\frac{r}{2\pi}} \tag{4}$$

where $\kappa_{\mathrm{tip}} = 3 - 4\nu_{\mathrm{tip}}$ for plane strain, $\kappa_{\mathrm{tip}} = (3 - \nu_{\mathrm{tip}})/(1 + \nu_{\mathrm{tip}})$ for plane stress, and ν_{tip} denotes the Poisson's ratio at the crack tip location. By correlating Equations (3) and (4), the SIF for mode I can be evaluated by

$$K_{\mathrm{I}} = \sqrt{\frac{2\pi}{\Delta a}} \left[4 \left(\frac{\mu}{\kappa + 1} \right)_{\mathrm{tip}} u_{2,i-1} - \left(\frac{\mu}{\kappa + 1} \right)_{\mathrm{tip}} u_{2,i-2} \right] \tag{5}$$

For mode II, the crack sliding displacement (CSD) replaces the COD and the following expression is obtained:

$$K_{\mathrm{II}} = \sqrt{\frac{2\pi}{\Delta a}} \left[4 \left(\frac{\mu}{\kappa + 1} \right)_{\mathrm{tip}} u_{1,i-1} - \left(\frac{\mu}{\kappa + 1} \right)_{\mathrm{tip}} u_{1,i-2} \right] \tag{6}$$

Note that in the above expressions for SIFs, the material properties ($\mu \equiv \mu(\mathbf{x})$ and $\kappa \equiv \kappa(\mathbf{x})$) have been taken at the crack tip location, which is consistent with Equation (2).

4. MODIFIED CRACK-CLOSURE (MCC) INTEGRAL FOR FGMs

The modified crack-closure integral method was proposed by Rybicki and Kanninen [27] based on Irwin's virtual crack-closure method [28] using the stresses ahead of the crack tip and the displacements behind the crack tip. The energy release rates can be obtained for modes I and II separately by this method, which utilizes only a single finite element analysis. No assumption of isotropy or homogeneity around the crack is necessary. Thus the method is ideally suited for FGMs. The energy release rate is estimated only in terms of the work done by the stresses (or equivalent nodal forces) over the displacements produced by the introduction of a virtual crack extension. The expression for $\mathscr{G}_{\mathrm{I}}$ (strain energy release rate for mode I) and $\mathscr{G}_{\mathrm{II}}$ (strain energy release rate for mode II) may be obtained according to Irwin [28] as

$$\mathscr{G}_{\mathrm{I}} = \lim_{\delta a \to 0} \frac{2}{\delta a} \int_{x_1 = 0}^{x_1 = \delta a} \frac{1}{2} \sigma_{22}(r = x_1, \theta = 0, a)\ u_2(r = \delta a - x_1, \theta = \pi, a + \delta a)\, \mathrm{d}x_1 \tag{7}$$

$$\mathscr{G}_{\mathrm{II}} = \lim_{\delta a \to 0} \frac{2}{\delta a} \int_{x_1 = 0}^{x_1 = \delta a} \frac{1}{2} \sigma_{12}(r = x_1, \theta = 0, a)\ u_1(r = \delta a - x_1, \theta = \pi, a + \delta a)\, \mathrm{d}x_1 \tag{8}$$

where $\sigma_{12} \equiv \sigma_{xy}$ and $\sigma_{22} \equiv \sigma_{yy}$ are shear and normal stresses ahead of the crack tip, and $u_1 \equiv u_x$ and $u_2 \equiv u_y$ are the relative displacements with respect to the crack tip co-ordinates, respectively. Figure 3 illustrates a self-similar virtual crack extension δa and the distribution of normal stress ahead of the crack tip.

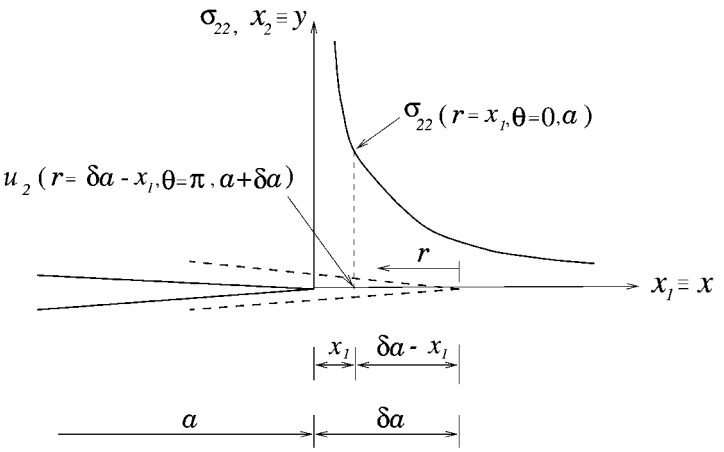

Figure 3. Self-similiar crack extension and normal stress distribution.

Stress intensity factors can be related to the values of the potential energy release rates through the following expressions [29]:

$$\mathcal{G}_{\mathrm{I}} = \left(\frac{\kappa+1}{8\mu}\right)_{\mathrm{tip}} K_{\mathrm{I}}^2 \quad \text{and} \quad \mathcal{G}_{\mathrm{II}} = \left(\frac{\kappa+1}{8\mu}\right)_{\mathrm{tip}} K_{\mathrm{II}}^2 \tag{9}$$

Ramamurthy *et al.* [30], and Raju [31] have shown that the values of $\mathcal{G}_{\mathrm{I}}$ and $\mathcal{G}_{\mathrm{II}}$ can be written in terms of the equivalent nodal forces $F_2 \equiv F_y$ and $F_1 \equiv F_x$, and the relative nodal displacements u_2 and u_1 when employing quarter-point singular elements around the crack tip (see Figure 2). They provided initial expressions for $\mathcal{G}_{\mathrm{I}}$ and $\mathcal{G}_{\mathrm{II}}$ which were valid only for pure mode, homogeneous problems. In general, for mixed mode problems, the deformation is neither symmetric nor antisymmetric about the local x_1-axis. Thus Raju [31] proposed the corrected formulae as follows:

$$\begin{aligned}\mathcal{G}_{\mathrm{I}} = \frac{1}{2\Delta a}[&F_{2,i}(t_{11}u_{2,i-2} + t_{12}u_{2,i-1}) + F_{2,i+1}(t_{21}u_{2,i-2} + t_{22}u_{2,i-1}) \\ &+ F_{2,i+2}^{\mathrm{T}}(t_{31}\bar{u}_{2,i-2} + t_{32}\bar{u}_{2,i-1}) + F_{2,i+2}^{\mathrm{B}}(t_{31}\hat{u}_{2,i-2} + t_{32}\hat{u}_{2,i-1})]\end{aligned} \tag{10}$$

$$\begin{aligned}\mathcal{G}_{\mathrm{II}} = \frac{1}{2\Delta a}[&F_{1,i}(t_{11}u_{1,i-2} + t_{12}u_{1,i-1}) + F_{1,i+1}(t_{21}u_{1,i-2} + t_{22}u_{1,i-1}) \\ &+ F_{1,i+2}^{\mathrm{T}}(t_{31}\bar{u}_{1,i-2} + t_{32}\bar{u}_{1,i-1}) + F_{1,i+2}^{\mathrm{B}}(t_{31}\hat{u}_{1,i-2} + t_{32}\hat{u}_{1,i-1})]\end{aligned}$$

where the first subscript in F or u refers to the Cartesian co-ordinate ($x_1 \equiv x$ or $x_2 \equiv y$) and the second subscript refers to the nodal point, the parameters t_{kl} ($k = 1, 2, 3;\ l = 1, 2$) are

given by

$$
\begin{aligned}
t_{11} &= 14 - \frac{33\pi}{8}, \qquad & t_{12} &= -52 - \frac{33\pi}{2} \\
t_{21} &= -\frac{7}{2} + \frac{21\pi}{16}, \qquad & t_{22} &= 17 - \frac{21\pi}{4} \\
t_{31} &= 8 - \frac{21\pi}{8}, \qquad & t_{32} &= -32 + \frac{21\pi}{2}
\end{aligned} \tag{11}
$$

and Δa is the characteristic length of singular elements around the crack tip which are six-node quarter-point triangular elements as illustrated in Figure 2. The superscripts T and B indicate the top and bottom regions of the crack with respect to x_1-axis, and thus F^{T} and F^{B} indicate the forces at top and bottom surfaces, respectively. The fields $\bar{u}$ and $\hat{u}$ represent the relative displacement of the top and bottom parts with respect to the crack tip. For example, at location $(i-1)$, $\bar{u}_{y,i-1} = v^{\mathrm{T}}_{y,i-1} - v_{y,i}$ and $\hat{u}_y = v^{\mathrm{B}}_{y,i-1} - v_{y,i}$ where v represents absolute displacement.

5. J_k^*-INTEGRAL FOR FGMs

This section presents a general derivation (for two-dimensional problems) of the J_k^* integral for non-homogeneous materials and details the actual FEM implementation in this work. The spatial variation of both elastic properties ($E \equiv E(\mathbf{x}), \nu \equiv \nu(\mathbf{x})$) is considered and the equivalent domain integral (EDI) concept is used to evaluate J_k^* $(k = 1, 2)$ in the FEM implementation. The presentation below is an extension of the J_k^* formulation by Eischen [15, 33]. Because of some previous controversy in the literature, a few words about the path independence of J_k^* are in order. Herrmann [32] has claimed that J_2 is path-dependent for paths surrounding the crack tip, however, Eischen [33] has shown that path independency of J_2 can be assured by including the integration of the strain energy density W along the lower and upper crack faces. Thus a correct definition of J_2 assuring path independency is obtained. The path independency of J_1 and J_2 ensures reliable computation of mixed mode SIFs. This will be demonstrated in the section on computational results by means of several numerical examples.

5.1. Formulation

An elastic body subjected to two dimensional deformation fields (plane strain, generalized plane stress) possesses a strain energy function W defined by

$$
W = W(\varepsilon_{ij}, x_i) \quad \text{where } \sigma_{ij} = \frac{\partial W}{\partial \varepsilon_{ij}} \ \ (i, j = 1, 2) \tag{12}
$$

To derive a balance law, the gradient of W needs to be evaluated, i.e.

$$
\frac{\partial W}{\partial x_k} = \frac{\partial W}{\partial \varepsilon_{ij}} \frac{\partial \varepsilon_{ij}}{\partial x_k} + \left(\frac{\partial W}{\partial x_k} \right)_{\mathrm{expl}} = \sigma_{ij} \varepsilon_{ij,k} + (W_{,k})_{\mathrm{expl}} \tag{13}
$$

where $(\cdot)_{,k} \equiv \partial(\cdot)/\partial x_k$, and the 'explicit' derivative of W is defined by

$$\left(\frac{\partial W}{\partial x_k}\right)_{\text{expl}} = \frac{\partial}{\partial x_k} W(\varepsilon_{ij}, x_i)\bigg|_{\varepsilon_{ij}=\text{const.},\ x_m=\text{const. for } m\neq k} \tag{14}$$

Using the symmetry properties of the stress tensor, the linearized strain–displacement relation, and the equilibrium equations, one obtains

$$(W\delta_{jk} - \sigma_{ij}u_{i,k})_{,j} - (W_{,k})_{\text{expl}} = 0 \tag{15}$$

where δ_{jk} is the Kronecker delta. This represents a balance law, valid pointwise, for an elastic FGM. A simple closed curve Γ in the (x_1, x_2) local plane is introduced along with the domain Ω which it encloses. By integrating Equation (15) over the domain Ω and applying the divergence theorem, the following expression is obtained:

$$\oint_\Gamma (Wn_k - \sigma_{ij}n_j u_{i,k})\,\mathrm{d}\Gamma - \int_\Omega (W_{,k})_{\text{expl}}\,\mathrm{d}\Omega = 0 \tag{16}$$

where n_j is the outward unit normal vector to Γ. For a linear elastic FGM, the strain energy function is

$$W = \tfrac{1}{2} C_{prst}(x_1, x_2) u_{p,r}\ u_{s,t} \tag{17}$$

where $C_{prst} = \lambda(\mathbf{x})\ \delta_{pr}\delta_{st} + \mu(\mathbf{x})\ (\delta_{ps}\delta_{rt} + \delta_{pt}\delta_{rs})$ denotes the elastic tensor, in which λ and μ are the Lame's moduli. Thus, for an isotropic FGM, the 'explicit' derivative of W is obtained in closed form as

$$(W_{,k})_{\text{expl}} = \tfrac{1}{2}[\lambda_{,k}\delta_{pr}\delta_{st} + \mu_{,k}(\delta_{ps}\delta_{rt} + \delta_{pt}\delta_{rs})]u_{p,r}u_{s,t} \tag{18}$$

Since the stress and strain fields are singular at a crack tip, and therefore unbounded, the region Ω in Equation (16) should not contain the crack tip. In order to derive an integral expression which is valid in the presence of a crack tip, a special region Ω must be considered. Figure 4 shows a crack located in a two-dimensional body of arbitrary shape. The region Ω (free of singularity) is bounded by a closed curve Γ composed of segments Γ_0, Γ_c^+, Γ_ε, Γ_c^- as shown. The region between Γ_ε and the crack surfaces is Ω_ε. The region Ω_0 is defined as $\Omega + \Omega_\varepsilon$. The divergence theorem can be applied in the region Ω. Thus Equation (16) leads to

$$\int_{\Gamma_0} b_k\,\mathrm{d}\Gamma + \int_{\Gamma_c^+} b_k\,\mathrm{d}\Gamma + \int_{\Gamma_\varepsilon} b_k\,\mathrm{d}\Gamma + \int_{\Gamma_c^-} b_k\,\mathrm{d}\Gamma - \int_\Omega (W_{,k})_{\text{expl}}\,\mathrm{d}\Omega = 0 \tag{19}$$

where

$$b_k = Wn_k - \sigma_{ij}n_j u_{i,k} \tag{20}$$

If the direction of integration is reversed in the third term of Equation (19), and the region Ω is decomposed into $\Omega_0 - \Omega_\varepsilon$, i.e. $\Omega = \Omega_0 - \Omega_\varepsilon$, it follows that

$$\int_{\Gamma_0} b_k\,\mathrm{d}\Gamma - \int_{\Omega_0} (W_{,k})_{\text{expl}}\,\mathrm{d}\Omega + \int_{\Gamma_c^+} b_k\,\mathrm{d}\Gamma + \int_{\Gamma_c^-} b_k\,\mathrm{d}\Gamma = \int_{\Gamma_\varepsilon} b_k\,\mathrm{d}\Gamma - \int_{\Omega_\varepsilon} (W_{,k})_{\text{expl}}\,\mathrm{d}\Omega \tag{21}$$

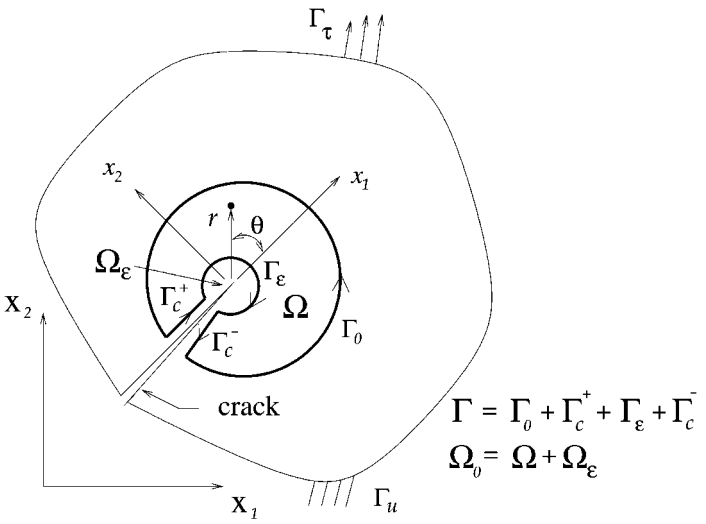

Figure 4. Schematic of cracked body.

A vector J_k^* is introduced as the limit $\Gamma_\varepsilon \to 0$ of the right-hand side of Equation (21), i.e.

$$J_k^* \equiv \lim_{\Gamma_\varepsilon \to 0} \left[\int_{\Gamma_\varepsilon} (W n_k - \sigma_{ij} n_j u_{i,k}) \, \mathrm{d}\Gamma - \int_{\Omega_\varepsilon} (W_{,k})_{\text{expl}} \, \mathrm{d}\Omega \right]$$

$$= \lim_{\Gamma_\varepsilon \to 0} \left[\int_{\Gamma_\varepsilon} b_k \, \mathrm{d}\Gamma - \int_{\Omega_\varepsilon} (W_{,k})_{\text{expl}} \, \mathrm{d}\Omega \right] \tag{22}$$

As the loop Γ_ε is shrunk onto the crack tip, the domain integral in Equation (22) vanishes because derivatives of the elastic moduli are assumed to be bounded at the crack tip. Then Equations (21) and (22) can be combined to produce

$$J_k^* \equiv \lim_{\Gamma_\varepsilon \to 0} \int_{\Gamma_\varepsilon} b_k \, \mathrm{d}\Gamma$$

$$= \lim_{\Gamma_\varepsilon \to 0} \left\{ \int_{\Gamma_0} b_k \, \mathrm{d}\Gamma - \int_{\Omega_0} (W_{,k})_{\text{expl}} \, \mathrm{d}\Omega + \int_{\Gamma_c^+} b_k \, \mathrm{d}\Gamma + \int_{\Gamma_c^-} b_k \, \mathrm{d}\Gamma \right\} \tag{23}$$

It is convenient to combine the two terms involving integration along the crack faces, and call the associated path of integration Γ_c. In order to combine these terms, the path Γ_0 must intersect the top and bottom crack faces which are at the same distance from the crack tip, as shown in Figure 4. Equation (23), together with Equation (20), leads to the

general expression

$$J_k^* = \lim_{\Gamma_\varepsilon \to 0} \left\{ \int_{\Gamma_0} [W n_k - \sigma_{ij} n_j u_{i,k}] \, \mathrm{d}\Gamma - \int_{\Omega_0} (W_{,k})_{\mathrm{expl}} \, \mathrm{d}\Omega \right.$$
$$\left. + \int_{\Gamma_c} ([W^+ - W^-] n_k^+ - [t_i^+ u_{i,k}^+ - t_i^- u_{i,k}^-]) \right\} \mathrm{d}\Gamma \tag{24}$$

where $t_i = \sigma_{ij} n_j$, $(+)$ and $(-)$ refer to the upper and lower crack faces, and $n_k^+ = -n_k^-$ is the outward unit normal vector to Γ_c^+. The notation $[W^+ - W^-]$ denotes the discontinuity (or jump) in the strain energy density across the crack opening. Notice that the material nonhomogeneity affects the standard J-integral [34] by adding a domain integral term. *This term must be accounted so that relatively large regions can be used to evaluate the J-integral in the FEM.*

By introducing the EDI [16, 35], the closed contour integral of Equation (24) can be converted to the following expression if the crack surfaces are assumed to be traction-free:

$$J_k^* = \int_A [\sigma_{ij} \; u_{i,k} - W \delta_{kj}] q_{,j} \, \mathrm{d}A - \int_A (W_{,k})_{\mathrm{expl}} \, q \, \mathrm{d}A + \int_{\Gamma_c} [W^+ - W^-] q n_k^+ \, \mathrm{d}\Gamma \tag{25}$$

where q is a smooth function which has the value of unity on Γ_ε and zero on Γ_0, and q was employed on the contour Γ_c [35]. The two often used shapes of the q function are the pyramid function and the plateau function. The plateau function was adopted in the present finite element analysis. For simplicity, let us define the last term of Equation (25) as

$$R = \int_{\Gamma_c} [W^+ - W^-] q n_k^+ \, \mathrm{d}\Gamma \tag{26}$$

where strain energy density can be represented as

$$W = W[E(\mathbf{x}), \nu(\mathbf{x}), \varepsilon(\mathbf{x})] \tag{27}$$

with $\mathbf{x} = (x_1, x_2)$.

Thus the derivative of W in the second term of Equation (25) becomes

$$\left(\frac{\partial W}{\partial x_k} \right)_{\mathrm{expl}} = \frac{\partial W}{\partial E} \frac{\partial E}{\partial x_k} + \frac{\partial W}{\partial \nu} \frac{\partial \nu}{\partial x_k} \tag{28}$$

If we separate Equation (25) into modes I and II, then for mode I ($k = 1$ in Equation (25)),

$$(J_1^*)_{\mathrm{local}} = \int_A [\sigma_{ij} u_{i,1} - W \delta_{1j}] \frac{\partial q}{\partial x_j} \, \mathrm{d}A - \int_A (W_{,1}) q \, \mathrm{d}A \tag{29}$$

and for mode II ($k = 2$ in Equation (25)),

$$(J_2^*)_{\mathrm{local}} = \int_A [\sigma_{ij} u_{i,2} - W \delta_{2j}] \frac{\partial q}{\partial x_j} \, \mathrm{d}A - \int_A (W_{,2}) q \, \mathrm{d}A + \int_{\Gamma_c} [W^+ - W^-] q n_2^+ \, \mathrm{d}\Gamma \tag{30}$$

Notice that the expression for $(J_2^*)_{\mathrm{local}}$ given in Equation (30) includes the term R which is the integration along the crack face of the discontinuity in the strain energy density, while

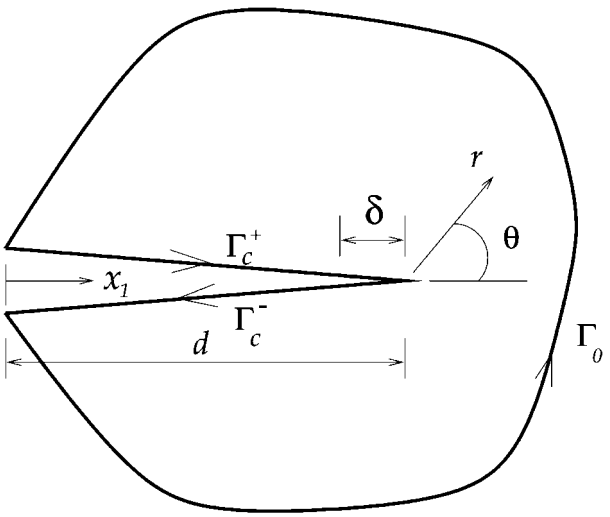

Figure 5. Schematic of the integration path.

the expression for $(J_1^*)_{\text{local}}$ does not. This term causes difficulty in numerical evaluation of $(J_2^*)_{\text{local}}$. In what follows, it is useful to derive an expression for $[W^+ - W^-]$ near a crack tip. The expressions for stresses near a crack tip in FGMs are given in Equation (1).

Recall that for plane stress in FGMs $(E \equiv E(\mathbf{x}), v \equiv v(\mathbf{x}))$

$$W = \frac{1}{2E(\mathbf{x})}(\sigma_{11}^2 + \sigma_{22}^2 - 2v(\mathbf{x})\sigma_{11}\sigma_{22}) + \frac{1+v(\mathbf{x})}{E(\mathbf{x})}\sigma_{12}^2 \tag{31}$$

Substituting Equation (1) into Equation (31) and performing some algebraic manipulation, one obtains

$$W(r,\pi) - W(r,-\pi) = [W^+ - W^-] = \frac{-4K_{\text{II}}\sigma_{x0}}{E(r)\sqrt{2\pi r}} + O(r^{1/2}) + \cdots \tag{32}$$

The range of integration can be divided into two parts, the first remote from the crack tip, and the second close to the crack tip. Thus a characteristic distance parameter is introduced, denoted by δ, as shown in Figure 5.

Hence, the origin of the x_1-axis will be located at the point where the path Γ_0 intersects the crack face. The distance from this point to the crack tip is d. It will be assumed that over the distance δ, the term $[W^+ - W^-]$ is satisfactorily approximated by the asymptotic form above (see Equation (32)). The following approximation is made to the integration of $[W^+ - W^-]$ along the crack face:

$$\begin{aligned}\int_{\Gamma_c} [W^+ - W^-] q n_2^+ \, \mathrm{d}\Gamma &= -\int_{\Gamma_c} [W^+ - W^-] q \, \mathrm{d}x_1 \\ &\approx -\int_0^{d-\delta} [W^+ - W^-] q \, \mathrm{d}x_1 - \int_{d-\delta}^{d} \frac{-4K_{\text{II}}\sigma_{x0}}{E_{\text{tip}}\sqrt{2\pi r}} q \, \mathrm{d}x_1 \end{aligned} \tag{33}$$

Using the fact that along the crack face $r = d - x_1$ (see Figure 5), one can evaluate the last integral in Equation (33) so that it can be written as

$$\int_{\Gamma_c} [W^+ - W^-] q n_2^+ \, \mathrm{d}\Gamma \approx - \int_0^{d-\delta} [W^+ - W^-] q \, \mathrm{d}x_1 + \frac{8 K_{\mathrm{II}} \sigma_{x0} \sqrt{\delta}}{E_{\mathrm{tip}} \sqrt{2\pi}} \tag{34}$$

Thus, based on Equation (30) and using the result given by Equation (34), the approximate expression for $(J_2^*)_{\mathrm{local}}$ is

$$\begin{aligned} (J_2^*)_{\mathrm{local}} \approx & \int_A [\sigma_{ij} u_{i,2} - W \delta_{2j}] \frac{\partial q}{\partial x_j} \, \mathrm{d}A - \int_A (W_{,2}) q \, \mathrm{d}A \\ & - \int_0^{d-\delta} [W^+ - W^-] q \, \mathrm{d}x_1 + \frac{8 K_{\mathrm{II}} \sigma_{x0} \sqrt{\delta}}{E_{\mathrm{tip}} \sqrt{2\pi}} \end{aligned} \tag{35}$$

If the crack faces are traction-free, an expression for the strain energy density can be obtained either according to the local co-ordinates (x_1, x_2), i.e. $W = (\sigma_{11} \varepsilon_{11})/2 = (E(x_1, x_2) \varepsilon_{11}^2)/2$ or to the global co-ordinates (X_1, X_2)

$$W = \tfrac{1}{2} (\sigma_{11} \varepsilon_{11} + \sigma_{22} \varepsilon_{22} + \sigma_{12} \varepsilon_{12}) \tag{36}$$

as used in the FEM implementation. The strain and stress values are evaluated directly (rather than being smoothed from the element interiors) on the crack faces (Γ_c^+ and Γ_c^-) by computing the strain–displacement matrix (**B** matrix) at those locations. Gauss quadrature along the 3-node line segments of the parent elements (T6, Q8) is used to integrate W. Such procedure improves the accuracy of the numerical results.

5.2. *Numerical aspects*

Since the FEM computations of displacement, strain, stress, etc., are based on the global co-ordinate system, the $(J_k^*)_{\mathrm{global}}$ is evaluated first and then transformed into $(J_k^*)_{\mathrm{local}}$. The quantity $(\hat{J}_2^*)_{\mathrm{local}}$ is introduced from Equation (35) as

$$(\hat{J}_2^*)_{\mathrm{local}} \approx \int_A [\sigma_{ij} u_{i,2} - W \delta_{2j}] \frac{\partial q}{\partial x_j} \, \mathrm{d}A - \int_A (W_{,2}) q \, \mathrm{d}A - \int_0^{d-\delta} [W^+ - W^-] q \, \mathrm{d}x_1 \tag{37}$$

so that

$$(J_2^*)_{\mathrm{local}} = (\hat{J}_2^*)_{\mathrm{local}} + \frac{8 K_{\mathrm{II}} \sigma_{x0} \sqrt{\delta}}{E_{\mathrm{tip}} \sqrt{2\pi}} \tag{38}$$

The relation among the two components of the J_k^*-integral and the mode I and mode II SIFs is established for plane stress as

$$(J_1^*)_{\mathrm{local}} = \frac{K_{\mathrm{I}}^2 + K_{\mathrm{II}}^2}{E_{\mathrm{tip}}} \tag{39}$$

$$(J_2^*)_{\mathrm{local}} = \frac{-2 K_{\mathrm{I}} K_{\mathrm{II}}}{E_{\mathrm{tip}}} \tag{40}$$

For plane strain, the Young's modulus at the crack tip E_{tip} must be divided by $(1 - v_{\text{tip}}^2)$, where v_{tip} denotes the Poisson's ratio at the crack tip. Upon examining Equations (38) and (40), it follows that

$$(\hat{J}_2^*)_{\text{local}} = -\frac{2K_{\text{I}}K_{\text{II}}}{E_{\text{tip}}} - \frac{8K_{\text{II}}\sigma_{x0}\sqrt{\delta}}{E_{\text{tip}}\sqrt{2\pi}} \tag{41}$$

The above expressions are represented by the local co-ordinates x_k, which can be expressed in terms of the global co-ordinates X_i by the usual transformation

$$x_i = \alpha_{ij}(\theta)X_j, \qquad \alpha_{ij}(\theta) = \begin{bmatrix} \cos\theta & \sin\theta \\ -\sin\theta & \cos\theta \end{bmatrix} \tag{42}$$

The same transformation also holds for the J_k^* integral, i.e.

$$\begin{Bmatrix} (J_1^*)_{\text{local}} \\ (J_2^*)_{\text{local}} \end{Bmatrix} = \begin{bmatrix} \cos\theta & \sin\theta \\ -\sin\theta & \cos\theta \end{bmatrix} \begin{Bmatrix} (J_1^*)_{\text{global}} \\ (J_2^*)_{\text{global}} \end{Bmatrix} \tag{43}$$

For the sake of numerical implementation by the FEM, Equation (25) is evaluated in global co-ordinates. Thus

$$(J_1^*)_{\text{global}} = (\tilde{J}_1^*)_{\text{global}} - R\sin\theta \tag{44}$$

$$(J_2^*)_{\text{global}} = (\tilde{J}_2^*)_{\text{global}} + R\cos\theta \tag{45}$$

where R is given by Equation (26) and

$$(\tilde{J}_1^*)_{\text{global}} = \int_A \left[\sigma_{ij}\frac{\partial u}{\partial X_1} - W\delta_{1j}\right]\frac{\partial q}{\partial X_j}\,\mathrm{d}A - \int_A \left(\frac{\partial W}{\partial X_1}\right) q\,\mathrm{d}A \tag{46}$$

$$(\tilde{J}_2^*)_{\text{global}} = \int_A \left[\sigma_{ij}\frac{\partial u}{\partial X_2} - W\delta_{2j}\right]\frac{\partial q}{\partial X_j}\,\mathrm{d}A - \int_A \left(\frac{\partial W}{\partial X_2}\right) q\,\mathrm{d}A \tag{47}$$

The defined quantities $(\tilde{J}_1^*)_{\text{global}}$ (Equation (46)) and $(\tilde{J}_2^*)_{\text{global}}$ (Equation (47)) are computed numerically to calculate $(J_1^*)_{\text{local}}$ according to the transformation given by Equation (43), i.e.

$$(J_1^*)_{\text{local}} = (\tilde{J}_1^*)_{\text{global}}\cos\theta + (\tilde{J}_2^*)_{\text{global}}\sin\theta \tag{48}$$

The quantity $(\hat{J}_2^*)_{\text{local}}$ is computed using Equation (37), for two values of δ (δ_1, δ_2). These values of $(\hat{J}_2^*)_{\text{local}}$ are called $(\hat{J}_2^*)_{\delta_1}$, and $(\hat{J}_2^*)_{\delta_2}$. Therefore, from Equation (41), one obtains

$$(\hat{J}_2^*)_{\delta_1} = -\frac{2K_{\text{I}}K_{\text{II}}}{E_{\text{tip}}} - \frac{8K_{\text{II}}\sigma_{x0}\sqrt{\delta_1}}{E_{\text{tip}}\sqrt{2\pi}} \tag{49}$$

$$(\hat{J}_2^*)_{\delta_2} = -\frac{2K_{\text{I}}K_{\text{II}}}{E_{\text{tip}}} - \frac{8K_{\text{II}}\sigma_{x0}\sqrt{\delta_2}}{E_{\text{tip}}\sqrt{2\pi}} \tag{50}$$

Once $(J_1^*)_{\text{local}}$, $(\hat{J}_2^*)_{\delta 1}$, and $(\hat{J}_2^*)_{\delta 2}$ have been computed numerically, Equations (39), (49), and (50) can be solved for K_{I}, K_{II}, and σ_{x0}. The solution is accomplished as follows:

$$-\frac{2K_{\text{I}}K_{\text{II}}}{E_{\text{tip}}} = (J_2^*)_{\text{local}} = \frac{(\hat{J}_2^*)_{\delta_1}\sqrt{\delta_2} - (\hat{J}_2^*)_{\delta_2}\sqrt{\delta_1}}{\sqrt{\delta_2} - \sqrt{\delta_1}} \tag{51}$$

$$-\frac{8K_{\text{II}}\sigma_{x0}}{E_{\text{tip}}\sqrt{2\pi}} = S = \frac{(\hat{J}_2^*)_{\delta_2} - (\hat{J}_2^*)_{\delta_1}}{\sqrt{\delta_2} - \sqrt{\delta_1}} \tag{52}$$

Then

$$K_{\text{I}} = \pm \left\{ \frac{E_{\text{tip}}(J_1^*)_{\text{local}}}{2} \left[1 \pm \left(1 - \left(\frac{(J_2^*)_{\text{local}}}{(J_1^*)_{\text{local}}} \right)^2 \right)^{1/2} \right] \right\}^{1/2} \tag{53}$$

$$K_{\text{II}} = \pm \left\{ \frac{E_{\text{tip}}(J_1^*)_{\text{local}}}{2} \left[1 \mp \left(1 - \left(\frac{(J_2^*)_{\text{local}}}{(J_1^*)_{\text{local}}} \right)^2 \right)^{1/2} \right] \right\}^{1/2} \tag{54}$$

The signs of K_{I} and K_{II} are determined by checking the magnitudes of the crack opening and sliding displacements near the crack tip. Such displacements are defined by

$$\Delta_{\text{I}} = u_2^+ - u_2^- \quad \text{and} \quad \Delta_{\text{II}} = u_1^+ - u_1^- \tag{55}$$

where, as before, the $(+)$ and $(-)$ refer to the upper and lower crack faces, respectively. The signs of K_{I} and K_{II} correspond to the signs of Δ_{I} and Δ_{II}, respectively. The sign of the term within the braces $[\cdot]$ in Equations (53) and (54) is determined by checking the following conditions:

$$\text{If} \quad |\Delta_{\text{I}}| \geqslant |\Delta_{\text{II}}| \quad \text{take } [+] \tag{56}$$

$$\text{If} \quad |\Delta_{\text{I}}| < |\Delta_{\text{II}}| \quad \text{take } [-] \tag{57}$$

Finally,

$$\sigma_{x0} = -\frac{\sqrt{2\pi}E_{\text{tip}}S}{8K_{\text{II}}} \tag{58}$$

The feasibility of the procedure explained above is illustrated in the section on numerical examples.

6. FINITE ELEMENT IMPLEMENTATION

The public domain FEM code FRANC2D (FRacture ANalysis Code 2D) [36, 37] has been used as the basic framework for implementing fracture capabilities in FGMs. It is worth

mentioning that the source code of FRANC2D is fully available—thus it is not a 'black box' (such as most commercial software), and this availability makes the code well suited for research investigations and for new developments. The code with extended capabilities for fracture of FGMs is called FGM_FRANC2D (Functionally Graded Material—FRacture ANalysis Code 2D). It considers spatial changes in material properties and special techniques to evaluate SIFs in FGMs such as J_k^*-integral, MCC and DCT, which were discussed in previous sections. The finite element stiffness equations can be written as [38]

$$\mathbf{k}^e\mathbf{u}^e = \mathbf{F}^e \tag{59}$$

with

$$\mathbf{k}^e = \int_{\Omega_e} \mathbf{B}^{e^{\mathrm{T}}}\mathbf{D}^e(\mathbf{x})\mathbf{B}^e \, \mathrm{d}\Omega_e \tag{60}$$

where $\mathbf{u}^e$ is the nodal displacement vector, $\mathbf{F}^e$ is the load vector, $\mathbf{B}^e$ is the strain–displacement matrix which contains gradients of the interpolating functions, $\mathbf{D}^e(\mathbf{x})$ is the constitutive matrix, and Ω_e is the domain of element (e). In the present work, the elasticity matrix $\mathbf{D}^e(\mathbf{x}) = \mathbf{D}^e(x_1, x_2)$ is assumed to be a function of spatial co-ordinates.

Two alternative approaches for graded elements have been considered and implemented: generalized isoparametric formulation and direct Gaussian integration. The quality of the graded elements has been investigated by Paulino and Kim [39] within the context of the weak patch test.

6.1. Generalized isoparametric formulation

In a standard parametric finite element formulation, displacements and co-ordinates are interpolated from the element nodal values. Similarly, material properties can also be interpolated from the element nodal values using shape functions. The general approach is illustrated as follows:

$$\text{Displacements } (u, v)\text{: e.g. } u = \sum_i N_i u_i \tag{61}$$

$$\text{Co-ordinates } (x, y)\text{: e.g. } x = \sum_i \tilde{N}_i x_i \tag{62}$$

$$\text{Material properties } (E, \nu)\text{: } E = \sum_i \bar{N}_i E_i; \quad \nu = \sum_i \hat{N}_i \nu_i \tag{63}$$

where N_i, $\tilde{N}_i$, $\bar{N}_i$, and $\hat{N}_i$ are shape functions corresponding to node i, and the summation is done over the element nodal points. Since the element formulation adopted here is fully isoparametric, then

$$\mathbf{N} = \tilde{\mathbf{N}} = \bar{\mathbf{N}} = \hat{\mathbf{N}} \tag{64}$$

In this approach, material properties at each Gaussian integration point are interpolated from the nodal material properties of the element using isoparametric shape functions, which are the same for spatial co-ordinates and displacements.

6.2. Direct Gaussian integration formulation

The integral in Equation (60) is evaluated by Gaussian quadrature, and the matrix $\mathbf{D}^e(\mathbf{x})$ is specified at each Gaussian integration point. Thus, for 2D problems, the resulting integral becomes

$$\mathbf{k}^e = \sum_{i=1}^{n} \sum_{j=1}^{n} \mathbf{B}_{ij}^{e^{\mathrm{T}}} \mathbf{D}_{ij}^e \mathbf{B}_{ij}^e J_{ij} w_i w_j \tag{65}$$

where the subscripts i and j refer to the Gaussian integration points, J_{ij} is the determinant of the Jacobian matrix, and w_i are the Gaussian weights.

7. COMPUTATIONAL RESULTS

One of the goals of this paper is to examine, by means of computational experiments, the elastic stress analysis for FGMs and the performance of the DCT, MCC, and J_k^*-integral methods for extracting SIFs in FGMs. In order to assess the various features of these methods, the following examples are presented:

(1) Edge crack in a plate.
(2) Slanted crack in a plate.
(3) Three-Point bending specimen with crack perpendicular to material gradation.
(4) Three-Point bending specimen with crack parallel to material gradation.
(5) Plate with an interior inclined crack.
(6) Multiple interacting cracks.

This set of problems comprise a severe test of the FEM code and the methods presented for evaluation of SIFs in FGMs. For quadratic (present work) and higher order elements, the two approaches discussed above (generalized isoparametric and direct Gaussian integration) are nearly equivalent. All the above problems have either experimental, numerical (e.g. finite element) or (semi-) analytical solutions available. Thus the results obtained with the FGM_FRANC2D code are compared against those available solutions.

7.1. Edge crack in a plate

Figure 6(a) shows an edge crack of length a located in a finite two-dimensional strip. Figures 6(b) and 6(c) show applied tension and bending loads, respectively, and Figure 6(d) shows a detail of the FEM mesh around the crack tip. The crack tip element size is $\Delta a = a/32$. This example was originally proposed by Erdogan and Wu [40], and it is one of the few theoretical fracture solutions available for a finite width FGM. The applied loading corresponds to $\sigma_{22}(x_1, \pm 4) = \pm 1.0$ for tension, and $\sigma_{22}(x_1, \pm 4) = \pm(-2x_1 + 1)$ for bending. This stress distribution was obtained by applying nodal forces along the top and bottom edges of the mesh. The displacement boundary condition is prescribed such that $u_2 = 0$ in the region $a \leqslant x_1 \leqslant 1$ along the $x_2 = 0$ line and, in addition, $u_1 = 0$ for the node at the right-hand side (see Figure 6(a)).

Young's modulus is an exponential function of x_1, i.e. $E(x_1) = E_1 \mathrm{e}^{\beta x_1}$, while Poisson's ratio is constant. The modulus variation, $E(x_1)$, is characterized by two parameters which

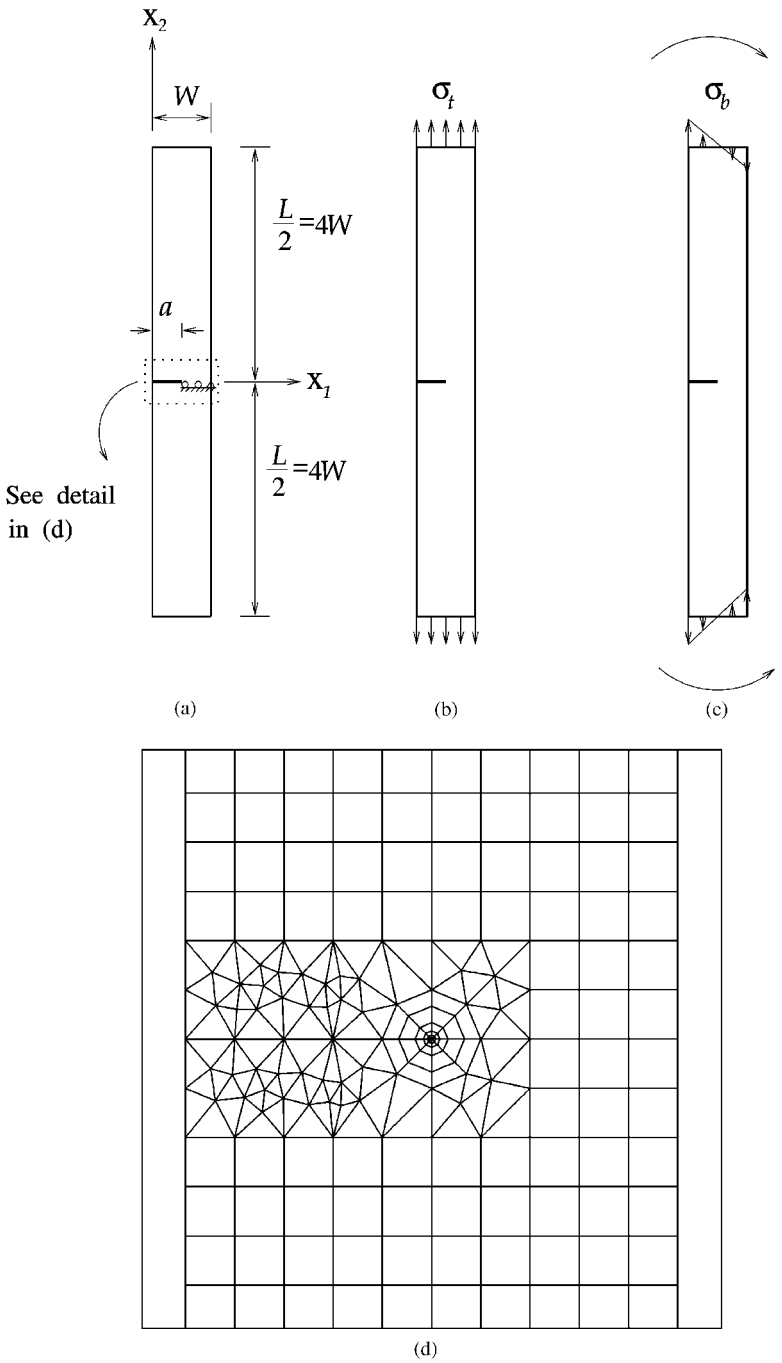

Figure 6. Configurations for edge cracked plate: (a) geometry and BCs; (b) tension loading; (c) bending loading; (d) detail of the FEM mesh around the crack tip showing eight sectors and five rings of elements.

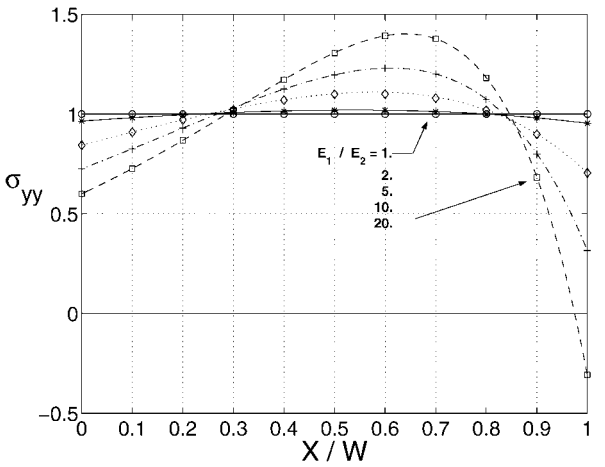

Figure 7. Stress distribution for *uncracked* strip under tension. Present (FEM) results are represented by data points. Erdogan and Wu's [40] results are represented by curved lines.

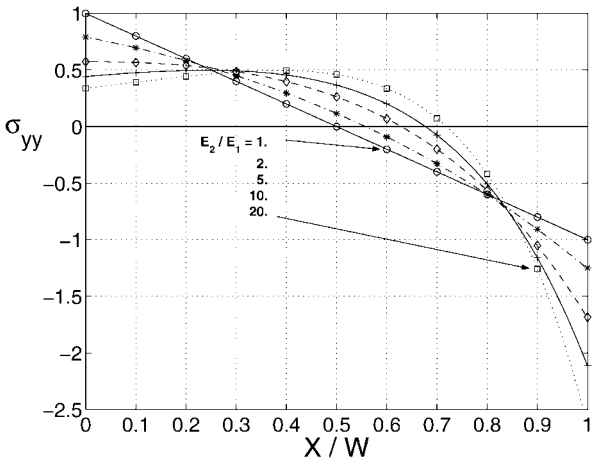

Figure 8. Stress distribution for *uncracked* strip under bending. Present (FEM) results are represented by data points. Erdogan and Wu's [40] results are represented by curved lines.

are selected to be $E_1 = E(0)$ and $E_2 = E(1)$ giving $\beta = \log(E_2/E_1)$. Eight-node serendipity elements (Q8) were used over most of the mesh, while around the crack tip, quarter-point six-node triangles (T6qp) were used. The typical mesh has 803 Q8, 124 T6 with a total of 927 elements and 2855 nodes. The following data were used for the finite element analysis: $a/W = 0.2, 0.3, 0.4, 0.5, 0.6; L/W = 8.0; E(x_1) = E_1 e^{\beta x_1} (E_1 = 1); E_2/E_1 = (0.1, 0.2, 1.0, 5.0, 10.0)$; $\nu = 0.3$; plane strain condition; and 2×2 Gauss quadrature.

For the tension and bending loads, Figures 7 and 8 show a comparison of the stress distributions in the uncracked plate between the FEM results and the analytical solution

Table I. Normalized stress intensity factors for edge cracked plate under tension.

Method	E_2/E_1	a/W 0.2	0.3	0.4	0.5	0.6
Erdogan and Wu [40]	0.1	1.296	1.858	2.569	3.570	5.188
	0.2	1.395	1.839	2.443	3.326	4.761
	1	N/A	N/A	N/A	N/A	N/A
	5	1.131	1.369	1.748	2.365	3.445
	10	1.001	1.229	1.588	2.176	3.212
Chen *et al.* [41]	0.1	1.366	1.926	2.658	3.666	5.243
	0.2	1.455	1.897	2.529	3.443	4.926
	1	1.408	1.698	2.178	2.933	4.237
	5	1.158	1.392	1.794	2.446	3.611
	10	1.032	1.249	1.614	2.223	3.337
MCC	0.1	1.280	1.832	2.523	3.470	4.921
	0.2	1.380	1.818	2.411	3.268	4.632
	1	1.358	1.649	2.097	2.806	4.005
	5	1.129	1.371	1.744	2.360	3.437
	10	1.001	1.234	1.582	2.174	3.207
$J_1^* \equiv J^*$	0.1	1.284	1.846	2.544	3.496	4.962
	0.2	1.390	1.831	2.431	3.292	4.669
	1	1.358	1.658	2.110	2.822	4.030
	5	1.132	1.370	1.749	2.366	3.448
	10	1.003	1.228	1.588	2.175	3.212
DCT	0.1	1.298	1.847	2.543	3.489	4.934
	0.2	1.396	1.832	2.429	3.286	4.644
	1	1.368	1.658	2.108	2.815	4.010
	5	1.132	1.366	1.744	2.375	3.426
	10	1.001	1.225	1.583	2.166	3.190

by Erdogan and Wu [40] (using strength of materials concepts). These figures show that both results agree within plotting accuracy. Thus such excellent results validate the present FEM implementation for elastic FGMs. Tables I and II compare the normalized SIFs for those two loading cases computed using DCT, MCC, and J_k^*-integral with those reported by Erdogan and Wu [40] and Chen *et al.* [41]. Using Erdogan and Wu's [40] results as reference, we observe that the J_k^*-integral method best estimates the Mode I SIFs for the mesh discretization of Figure 6. Moreover, for the exponential material variation used in this example, the explicit derivative of the strain energy density is $(W_{,1})_{\text{expl}} = \beta W$. Also the MCC and DCT show very good performance. However, the results by Chen *et al.* [41], using the element free Galerkin (EFG) method [42], are worse than ours, using the FEM (see Table I). Chen *et al.* [41] have discretized the plate (symmetric portion) with 617 nodes and they have also considered the explicit derivative term in the J_1^*-integral (see Equation (29)).

Table II. Normalized stress intensity factors for edge cracked plate under bending.

Method	E_2/E_1	a/W 0.2	0.3	0.4	0.5	0.6
Erdogan and Wu [40]	0.1	1.904	1.885	1.977	2.215	2.717
	0.2	1.595	1.612	1.721	1.953	2.403
	1	N/A	N/A	N/A	N/A	N/A
	5	0.687	0.777	0.923	1.151	1.559
	10	0.564	0.658	0.804	1.035	1.428
MCC	0.1	1.873	1.850	1.927	2.128	2.532
	0.2	1.575	1.590	1.693	1.910	2.322
	1	1.048	1.116	1.252	1.487	1.901
	5	0.685	0.776	0.921	1.156	1.557
	10	0.564	0.658	0.803	1.033	1.426
$J_1^* \equiv J^*$	0.1	1.888	1.864	1.943	2.145	2.553
	0.2	1.588	1.601	1.706	1.925	2.341
	1	1.055	1.122	1.260	1.496	1.913
	5	0.687	0.778	0.924	1.158	1.561
	10	0.565	0.659	0.804	1.035	1.429
DCT	0.1	1.880	1.855	1.930	2.127	2.536
	0.2	1.583	1.596	1.697	1.911	2.327
	1	1.053	1.120	1.256	1.488	1.903
	5	0.686	0.757	0.920	1.152	1.553
	10	0.564	0.656	0.800	1.028	1.421

7.2. *Slanted crack in a plate*

The slanted crack in a two-dimensional elastic body provides a mixed-mode loading situation which requires computation of both J_1^* and J_2^* in order to determine the SIFs. Figure 9(a) shows a slanted crack in a finite two-dimensional plate with three integration contours, and Figure 9(b) shows the mesh discretization, which is the same as the one adopted by Eischen [15], who proposed this problem. The applied load is prescribed along the upper edge with normal stress $\sigma_{22}(x_1, 1) = \bar{\varepsilon}\bar{E}e^{\beta(x_1-0.5)}$ where $\bar{\varepsilon} = 1$. The displacement boundary condition is specified such that $u_2 = 0$ along the lower edge and, in addition, $u_1 = 0$ for the node at the right-hand side.

The Young's modulus varies according to $E(x_1) = \bar{E}e^{\beta(x_1-0.5)}$, where $\bar{E} = 1.0$, $\beta a = 0.4\sqrt{2}$, and the Poisson's ratio is assumed to be constant. Eight-node serendipity quadrilateral elements (Q8) were used over most of the mesh, while near the crack tip quarter-point six-node triangles (T6qp) were utilized. The mesh has 97 Q8, 38 T6 with a total of 135 elements and 412 nodes. The following data were used for the finite element analysis: $a/W = 0.4\sqrt{2}$; $L/W = 2.0$; $E = 1.0$; $\nu = 0.3$; generalized plane stress; and 2×2 Gauss quadrature. Table III shows a comparison of the normalized SIFs and non-singular stress component using regions 2 and 3 (see Figure 9) with those obtained by Eischen [15]. The integration regions 2 and 3 provide the same converged SIFs. The results in Table III indicate resonably good agreement between ours and Eischen's [15] solution for this problem.

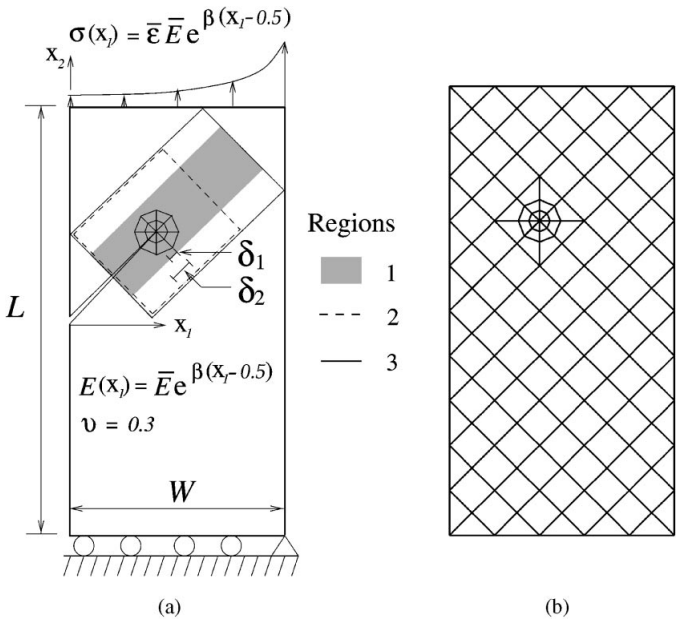

Figure 9. Slanted crack plate configuration: (a) geometry, BCs, J_k^*-integral parameters (δ_1, δ_2) and integration regions 1–3; (b) FEM mesh (same as the mesh used by Eischen [15]).

Table III. Normalized SIF and non-singular stress component for FGM slanted crack plate $(a/W = 0.4\sqrt{2},\ L/W = 2.0)$.

	Present results (J_k^*-Integral)			Eischen [15]		
βa	$K_{\mathrm{I}}/\bar{\varepsilon}\bar{E}\sqrt{\pi a}$	$K_{\mathrm{II}}/\bar{\varepsilon}\bar{E}\sqrt{\pi a}$	$\sigma_{x0}/\bar{\varepsilon}\bar{E}$	$K_{\mathrm{I}}/\bar{\varepsilon}\bar{E}\sqrt{\pi a}$	$K_{\mathrm{II}}/\bar{\varepsilon}\bar{E}\sqrt{\pi a}$	$\sigma_{x0}/\bar{\varepsilon}\bar{E}$
0.00	1.451	0.604	0.796	1.438	0.605	0.822
0.10	1.396	0.579	0.769	N/A	N/A	N/A
0.25	1.316	0.544	0.731	N/A	N/A	N/A
0.50	1.196	0.491	0.673	N/A	N/A	N/A
0.75	1.089	0.443	0.620	N/A	N/A	N/A
1.00	0.993	0.402	0.572	0.984	0.395	0.588

7.3. Three-point bending specimen with crack perpendicular to material gradation

Marur and Tippur [43] have fabricated FGM specimens using gravity assisted casting technique with two-part slow curing epoxy and uncoated solid glass sphere fillers. They have also analysed a three-point bending specimen with a crack normal to the elastic gradient using both experimental (static fracture tests) and numerical (FEM) techniques [18]. Figure 10(a) shows the specimen geometry and BCs. Figure 10(b) shows linear variation of Young's modulus in the material gradient region from 10.79 to 3.49 GPa, and linear variation of

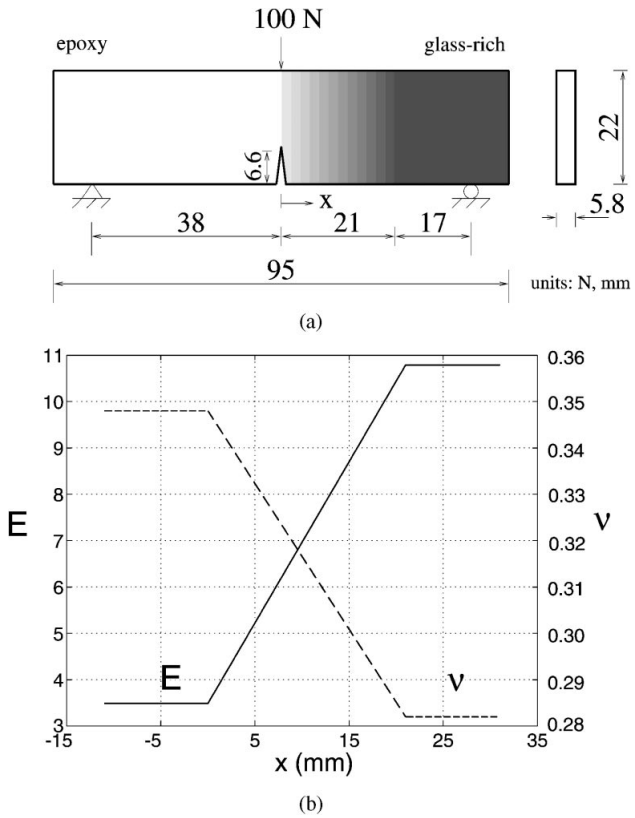

Figure 10. Three-point bending specimen with crack perpendicular to the material gradation: (a) specimen geometry (length in mm); (b) variation of Young's modulus and Poisson's ratio.

Poisson's ratio from 0.348 for epoxy side to 0.282 for glass-rich side. Figure 11(a) shows the global FEM mesh configuration, and Figure 11(b) shows a detail of the mesh using 16 sectors around the crack tip. Marur and Tippur [18] used the experimental strain data to compute $|\mathbf{K}| = 0.65\,\mathrm{MPa}\sqrt{m}$ and $\psi = -3.45°$, while their FEM results are $|\mathbf{K}| = 0.59\,\mathrm{MPa}\sqrt{m}$ and $\psi = -3.24°$, where $\psi = \tan^{-1}(K_{\mathrm{II}}/K_{\mathrm{I}})$ is the mode-mixity parameter. These numerical results, together with the present ones using MCC, DCT, and J_k^*-integral, are reported in Table IV.

7.4. Three-point bending specimen with crack parallel to material gradation

Figure 12 shows the three-point bending specimen geometry and BCs. Figure 13(a) shows the global FEM mesh configuration, and Figure 13(b) shows a detail around the crack tip. The variation of Young's modulus in the material gradient region is linear and the Poisson's ratio is constant. If the origin of the Cartesian co-ordinates is located at the centre of the specimen and the x_2-axis is along the thickness direction, the Young's modulus is expressed by $E(x_2) = Ax_2 + B$, where $A = (E_2 - E_1)/2h$, and $B = (E_2 + E_1)/2$.

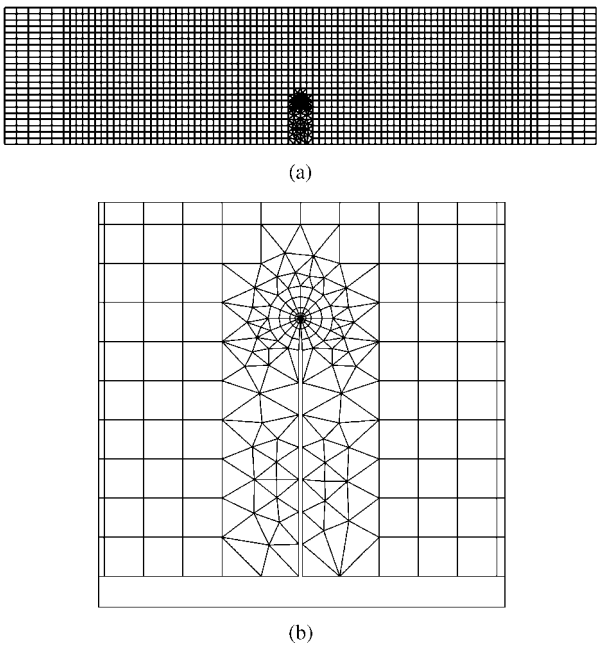

Figure 11. Finite element mesh for three-point bending specimen with crack perpendicular to the material gradation: (a) finite element mesh; (b) detail around the crack tip showing 16 sectors and four rings of elements.

Table IV. FEM SIFs for three-point bending specimen with crack perpendicular to material gradation.

Parameters	Present results			Marur and Tippur [18]
	MCC	J_k^*-integral	DCT	
K_{I}	0.557	0.557	0.558	0.589
K_{II}	−0.028	−0.026	−0.026	−0.033
$\lvert\mathbf{K}\rvert$	0.5575	0.5576	0.5580	0.59
ψ	−2.87°	−2.67°	−2.64°	−3.24°

Table V shows the solution for Mode I SIFs corresponding to crack tip position in the FGM for linear material variation, where $h/H = 0.1$. All the three methods provide consistent results with respect to each other and agree well with the results presented by Gu *et al.* [16] in graphic form.

7.5. Plate with an interior inclined crack

Figure 14 shows an interior inclined crack of length $2a$ located with angle θ in a finite two-dimensional plate, and Figure 15 shows mesh configurations with various crack slopes

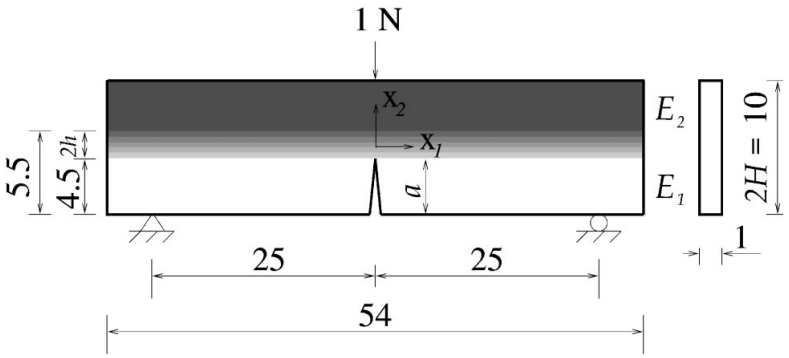

Figure 12. Single edge notched bend (SENB) specimen with crack parallel to material gradation.

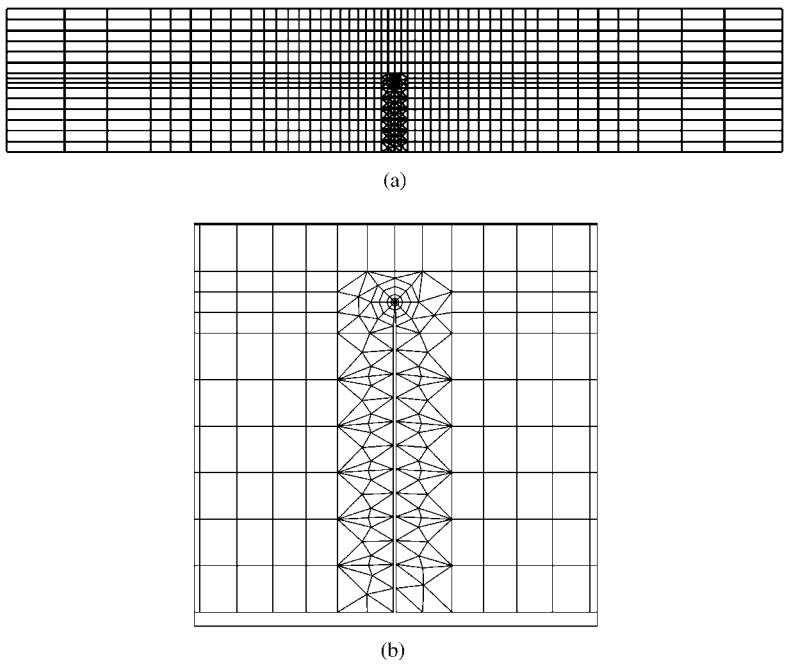

Figure 13. Finite element mesh for three point bending specimen with crack parallel to the material gradation: (a) finite element mesh; (b) detail around the crack tip showing eight sectors and five rings of elements.

measured clockwise. Konda and Erdogan [44] have investigated an infinite plate with such a configuration. The applied load corresponds to $\sigma_{22}(x_1, 10) = \bar{\varepsilon}\bar{E}e^{\beta x_1}$, and such stress distribution was obtained by applying nodal forces along the top edge of the mesh. The displacement boundary condition is prescribed such that $u_2 = 0$ along the lower edge and, in addition,

Table V. Normalized SIFs for three-point bending specimen with crack parallel to material gradation ($h/H = 0.1$).

	$K_1\sqrt{H}/P$ $(a = 4.5)$			$K_1\sqrt{H}/P$ $(a = 5.0)$			$K_1\sqrt{H}/P$ $(a = 5.5)$		
E_2/E_1	MCC	J_k^*-int	DCT	MCC	J_k^*-int	DCT	MCC	J_k^*-int	DCT
0.05	32.66	33.04	32.57	30.72	31.12	31.01	14.98	15.21	15.18
0.1	23.23	23.47	23.18	23.47	23.92	23.79	13.66	13.73	13.76
0.2	17.18	17.36	17.18	18.01	18.32	18.24	12.65	12.79	12.71
0.5	11.54	11.65	11.55	12.42	12.57	12.52	11.65	11.76	11.69
1	8.072	8.134	8.069	9.398	9.467	9.413	11.05	11.15	11.09
2	5.198	5.239	5.185	7.296	7.318	7.258	10.53	10.62	10.56
5	2.526	2.540	2.497	5.502	5.496	5.438	9.878	9.963	9.903
10	1.327	1.334	1.294	4.606	4.586	4.543	9.427	9.505	9.451
20	0.652	0.660	0.620	3.980	3.939	3.924	9.049	9.123	9.073

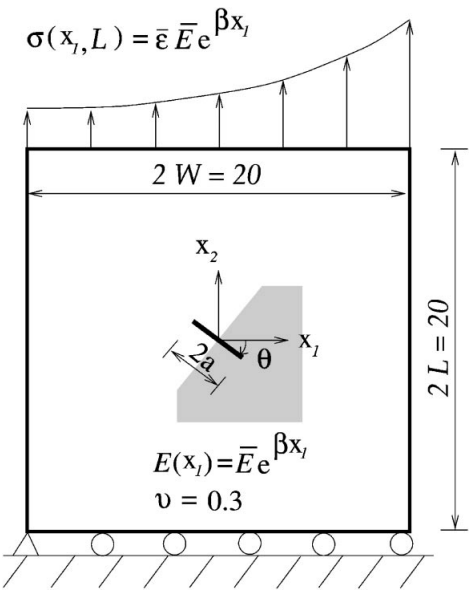

Figure 14. Plate with an inclined crack in which the angle θ is measured clockwise (cw) with respect to the Cartesian axes. The shaded area illustrates a typical region used for the EDI computation of J_k^*.

$u_1 = 0$ for the node at the left-hand side. This loading results in a uniform strain $\varepsilon_{11}(x_1, x_2) = \bar{\varepsilon}$ in a corresponding uncracked structure.

Young's modulus is an exponential function of x_1, while Poisson's ratio is constant. Eight-node serendipity elements (Q8) were used over most of the mesh, while at each crack tip, quarter-point six-node triangles (T6qp) were used. The following data were used for the FEM analysis: $a/W = 0.1$; $L/W = 1.0$; $E(x_1) = \bar{E}e^{\beta x_1}$; $\bar{E} = 1.0$; $\theta/\pi = (0, 0.1, 0.2, 0.3, 0.4, 0.5)$; $\beta a = (0.25, 0.5)$; $\bar{\varepsilon} = 1.0$; $v = 0.3$; generalized plane stress; and 2×2 Gauss quadrature. The

characteristic length Δa (see Figure 2) was selected such that $(\delta_1, \delta_2) = (a/18, a/9)$ for both $\beta a = 0.25$ and $\beta a = 0.5$. Tables VI and VII compare the normalized SIFs computed by using the DCT, the J_k^*-integral and the MCC with those reported by Konda and Erdogan [44]. The selection of a typical region for the EDI computation of J_k^* around the crack tip is illustrated by the shaded portion of Figure 14.

It can be observed that for pure mode I, the J_k^*-integral, the MCC, and the DCT provided good results within 4 per cent errors. For mixed-mode conditions, the MCC best estimates the SIFs within 6 per cent errors regardless of the choice of the characteristic lengths of the first ring of elements around the crack tips. The DCT also best estimates the SIFs within 6 per cent errors providing better results as the characteristic length becomes smaller. The J_k^*-integral shows relatively good performance within 9 per cent errors for $\Delta a = a/18$ and $\beta a = 0.25$ (Table VI) or $\beta a = 0.5$ (Table VII). For $\Delta a = a/9$ and $\beta a = 0.25$ (Table VI) or $\beta a = 0.5$ (Table VII), the general performance of the J_k^* method is also good, however, it deteriorates as the crack approaches the vertical orientation, i.e. $\theta/\pi \to 0.5$ in Tables VI and VII. Table VIII shows a comparison of the SIFs using J_k^*-integral with eight (S8) and sixteen (S16) sectors around the crack tips. The SIF results are similar to each other, indicating convergence of the results with respect to the number of sectors (relevant for better resolution of hoop stresses). It can also be observed that some numerical residuals were obtained for the MCC with a horizontal crack ($\theta = 0^\circ$) and the J_k^* with a vertical crack ($\theta = 90^\circ$), which are indicated by an $*$ in the tables of results.

7.6. *Multiple interacting cracks*

Figure 16(a) shows two cracks of length $2a$ located with the angle θ_i ($\theta_1 = 30^\circ$, $\theta_2 = 60^\circ$) in a finite two-dimensional plate. Figure 16(b) shows the complete FEM mesh, and Figures 16(c) and 16(d) show details of the centre region and around crack tips, respectively. The distance from the origin to the two crack tips is 1.0. Shbeeb *et al.* [45, 46] have provided semi-analytical solutions for this example obtained with the integral equation method. However, graphical results were given in their paper which makes accurate verification difficult. The applied load corresponds to $\sigma_{22}(x_1, \pm 10) = \pm\sigma_0 = 1.0$. This stress distribution was obtained by applying nodal forces along the top edge of the mesh. The displacement boundary condition is prescribed such that $u_2 = 0$ along the lower edge and, in addition, $u_1 = 0$ for the node at the left-hand side. Young's modulus is an exponential function of x_2, while Poisson's ratio is constant and is set to be zero in this numerical analysis. The actual value of the Poisson's ratio was not provided in the paper by Shbeeb *et al.* [46]. Eight-node serendipity elements (Q8) were used over most of the mesh, while at each crack tip, quarter-point six-node triangles (T6qp) were used. The mesh has 2287 Q8 and 214 T6 with a total of 2501 elements and 7517 nodes. The following data were used for the finite element analysis: $2a = 2$; $L/W = 1.0$; $E(x_2) = \bar{E}e^{\beta x_2}$; $\bar{E} = 1.0$; $\beta a = (0.0, 0.25, 0.5, 0.75, 1.0)$; $v = 0.0$; generalized plane stress; and 2×2 Gauss quadrature. With such geometrical configuration, the material property E can get out-of-bounds as the plate size increases. This occurs because the non-homogeneity parameter β introduces a geometrical length scale in the problem. The geometrical configuration for this problem was adopted simply as a means to approximate the infinite plate as originally conceived by Shbeeb *et al.* [46].

Table IX shows a comparison of the normalized SIFs at two crack tips for the lower crack with the angle $\theta = 30^\circ$ computed by using the DCT, MCC, the J_k^* integral with those reported

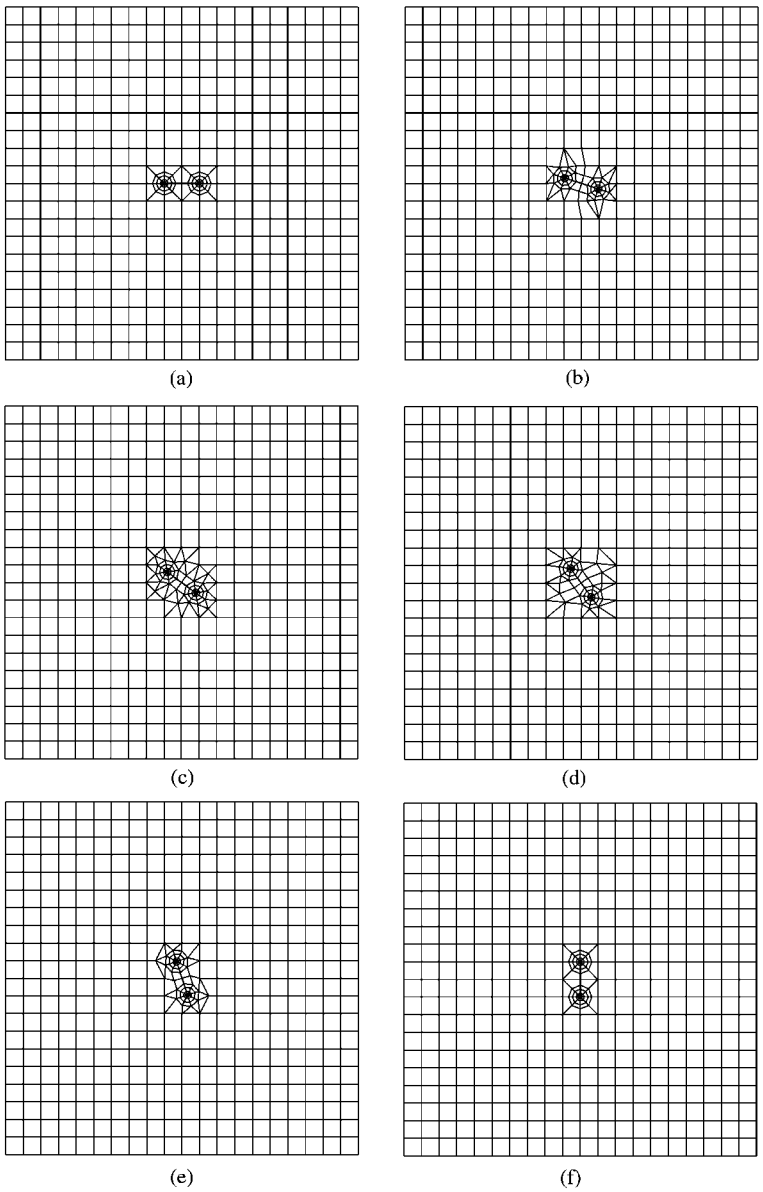

Figure 15. Mesh configurations with various crack slopes measured clockwise (cw): (a) $\theta = 0^\circ$; (b) $\theta = 18^\circ$; (c) $\theta = 36^\circ$; (d) $\theta = 54^\circ$; (e) $\theta = 72^\circ$; and (f) $\theta = 90^\circ$.

by Shbeeb *et al.* [45, 46]. In this table $K_{\mathrm{I}}(a^-)$ and $K_{\mathrm{I}}(a^+)$ refer to the SIFs at the left and right crack tips, respectively. Similar notation is adopted for K_{II}. It can be observed that both the DCT and J_k^*-integral agree reasonably well with the results by Shbeeb *et al.* [46], and the MCC best estimates the SIFs.

Table VI. Normalized stress intensity factors ($\beta a = 0.25,\ K_0 = \bar{E}\bar{\varepsilon}\sqrt{\pi a}$).

$\delta_1 = \Delta a$	Method	θ/π	$K_{\mathrm{I}}(a)/K_0$	$K_{\mathrm{II}}(a)/K_0$	$K_{\mathrm{I}}(-a)/K_0$	$K_{\mathrm{II}}(-a)/K_0$
	Konda and	0	1.196	0	0.825	0
	Erdogan	0.1	1.081	−0.321	0.750	−0.254
N/A	[44]	0.2	0.781	−0.514	0.548	−0.422
		0.3	0.414	−0.504	0.290	−0.437
		0.4	0.121	−0.304	0.075	−0.282
		0.5	0	0	0	0
	MCC	0	1.221	$\approx 0^*$	0.827	$\approx 0^*$
		0.1	1.101	−0.325	0.752	−0.250
		0.2	0.789	−0.519	0.549	−0.416
		0.3	0.414	−0.507	0.291	−0.432
		0.4	0.117	−0.303	0.073	−0.277
		0.5	0	0	0	0
	J_k^*-integral	0	1.220	0	0.840	0
		0.1	1.106	−0.315	0.769	−0.239
$a/9$		0.2	0.810	−0.494	0.582	−0.390
		0.3	0.404	−0.523	0.297	−0.439
		0.4	0.135	−0.304	0.097	−0.280
		0.5	$\approx 0^*$	0	$\approx 0^*$	0
	DCT	0	1.235	0	0.854	0
		0.1	1.140	−0.312	0.775	−0.248
		0.2	0.802	−0.499	0.565	−0.412
		0.3	0.423	−0.489	0.297	−0.425
		0.4	0.122	−0.293	0.075	−0.272
		0.5	0	0	0	0
	MCC	0	1.217	$\approx 0^*$	0.830	$\approx 0^*$
		0.1	1.098	−0.324	0.754	−0.252
		0.2	0.788	−0.516	0.551	−0.417
		0.3	0.414	−0.504	0.291	−0.432
		0.4	0.119	−0.302	0.075	−0.277
		0.5	0	0	0	0
	J_k^*-integral	0	1.220	0	0.840	0
		0.1	1.106	−0.317	0.767	−0.246
$a/18$		0.2	0.812	−0.492	0.578	−0.396
		0.3	0.390	−0.534	0.282	−0.449
		0.4	0.120	−0.311	0.079	−0.286
		0.5	$\approx 0^*$	0	$\approx 0^*$	0
	DCT	0	1.227	0	0.845	0
		0.1	1.107	−0.310	0.768	−0.245
		0.2	0.796	−0.496	0.560	−0.407
		0.3	0.420	−0.485	0.295	−0.420
		0.4	0.121	−0.291	0.075	−0.269
		0.5	0	0	0	0

*Numerical residual.

Table VII. Normalized stress intensity factors ($\beta a = 0.5,\ K_0 = \bar{E}\bar{\varepsilon}\sqrt{\pi a}$).

$\delta_1 = \Delta a$	Method	θ/π	$K_{\mathrm{I}}(a)/K_0$	$K_{\mathrm{II}}(a)/K_0$	$K_{\mathrm{I}}(-a)/K_0$	$K_{\mathrm{II}}(-a)/K_0$
	Konda and	0	1.424	0	0.674	0
	Erdogan	0.1	1.285	−0.344	0.617	−0.213
N/A	[44]	0.2	0.925	−0.548	0.460	−0.365
		0.3	0.490	−0.532	0.247	−0.397
		0.4	0.146	−0.314	0.059	−0.269
		0.5	0	0	0	0
	MCC	0	1.458	$\approx 0^*$	0.664	$\approx 0^*$
		0.1	1.310	−0.353	0.608	−0.207
		0.2	0.933	−0.558	0.454	−0.355
		0.3	0.487	−0.536	0.244	−0.386
		0.4	0.142	−0.312	0.059	−0.262
		0.5	0	0	0	0
	J_k^*-integral	0	1.446	0	0.679	0
		0.1	1.306	−0.341	0.628	−0.195
$a/9$		0.2	0.944	−0.534	0.488	−0.329
		0.3	0.461	−0.563	0.256	−0.392
		0.4	0.156	−0.314	0.083	−0.265
		0.5	$\approx 0^*$	0	$\approx 0^*$	0
	DCT	0	1.461	0	0.693	0
		0.1	1.315	−0.333	0.633	−0.209
		0.2	0.943	−0.529	0.469	−0.356
		0.3	0.498	−0.512	0.249	−0.384
		0.4	0.148	−0.301	0.058	−0.258
		0.5	0	0	0	0
	MCC	0	1.448	$\approx 0^*$	0.669	$\approx 0^*$
		0.1	1.302	−0.350	0.612	−0.209
		0.2	0.929	−0.552	0.456	−0.357
		0.3	0.487	−0.531	0.245	−0.388
		0.4	0.143	−0.310	0.059	−0.262
		0.5	0	0	0	0
	J_k^*-integral	0	1.446	0	0.679	0
		0.1	1.306	−0.341	0.625	−0.203
$a/18$		0.2	0.946	−0.531	0.483	−0.337
		0.3	0.446	−0.576	0.240	−0.402
		0.4	0.142	−0.321	0.064	−0.270
		0.5	$\approx 0^*$	0	$\approx 0^*$	0
	DCT	0	1.453	0	0.686	0
		0.1	1.308	−0.331	0.626	−0.205
		0.2	0.937	−0.526	0.465	−0.351
		0.3	0.494	−0.508	0.247	−0.379
		0.4	0.146	−0.299	0.058	−0.255
		0.5	0	0	0	0

*Numerical residual.

Table VIII. Comparison of normalized stress intensity factors for eight (S8) and 16 (S16) sectors ($\beta a = 0.5,\ K_0 = \bar{E}\bar{\varepsilon}\sqrt{\pi a}$).

$\delta_1 = \Delta a$	Method	θ/π	$K_{\mathrm{I}}(a)/K_0$	$K_{\mathrm{II}}(a)/K_0$	$K_{\mathrm{I}}(-a)/K_0$	$K_{\mathrm{II}}(-a)/K_0$
	Konda and	0	1.424	0	0.674	0
	Erdogan	0.1	1.285	−0.344	0.617	−0.213
N/A	[44]	0.2	0.925	−0.548	0.460	−0.365
		0.3	0.490	−0.532	0.247	−0.397
		0.4	0.146	−0.314	0.059	−0.269
		0.5	0	0	0	0
	J_k^*-integral	0	1.446	0	0.679	0
		0.1	1.306	−0.341	0.625	−0.203
$a/18$	S8	0.2	0.946	−0.531	0.483	−0.337
		0.3	0.446	−0.576	0.240	−0.402
		0.4	0.142	−0.321	0.064	−0.270
		0.5	$\approx 0^*$	0	$\approx 0^*$	0
	J_k^*-integral	0	1.453	0	0.684	0
		0.1	1.306	−0.350	0.625	−0.211
$a/18$	S16	0.2	0.950	−0.526	0.481	−0.339
		0.3	0.443	−0.579	0.244	−0.400
		0.4	0.149	−0.318	0.065	−0.270
		0.5	$\approx 0^*$	0	$\approx 0^*$	0

*Numerical residual.

Table IX. Normalized stress intensity factors for lower crack ($K_0 = \sigma_{22}\sqrt{\pi a}$).

Method	β	$K_{\mathrm{I}}(a^-)/K_0$	$K_{\mathrm{II}}(a^-)/K_0$	$K_{\mathrm{I}}(a^+)/K_0$	$K_{\mathrm{II}}(a^+)/K_0$
Shbeeb *et al.*	0.0	0.59	0.43	0.78	0.42
[46]	0.25	0.62	0.39	0.82	0.48
(Approximate)	0.5	0.66	0.36	0.88	0.57
	0.75	0.69	0.34	0.98	0.685
	1.0	0.70	0.315	1.10	N/A
MCC	0.0	0.589	0.423	0.804	0.408
	0.25	0.626	0.385	0.816	0.474
	0.5	0.662	0.346	0.842	0.546
	0.75	0.696	0.312	0.880	0.625
	1.0	0.715	0.277	0.930	0.709
J_k^*-integral	0.0	0.603	0.431	0.801	0.431
	0.25	0.627	0.401	0.811	0.495
	0.5	0.662	0.363	0.841	0.558
	0.75	0.692	0.347	0.895	0.617
	1.0	0.734	0.298	0.985	0.663
DCT	0.0	0.598	0.413	0.812	0.399
	0.25	0.632	0.375	0.818	0.463
	0.5	0.672	0.336	0.838	0.533
	0.75	0.712	0.302	0.869	0.610
	1.0	0.747	0.273	0.910	0.693

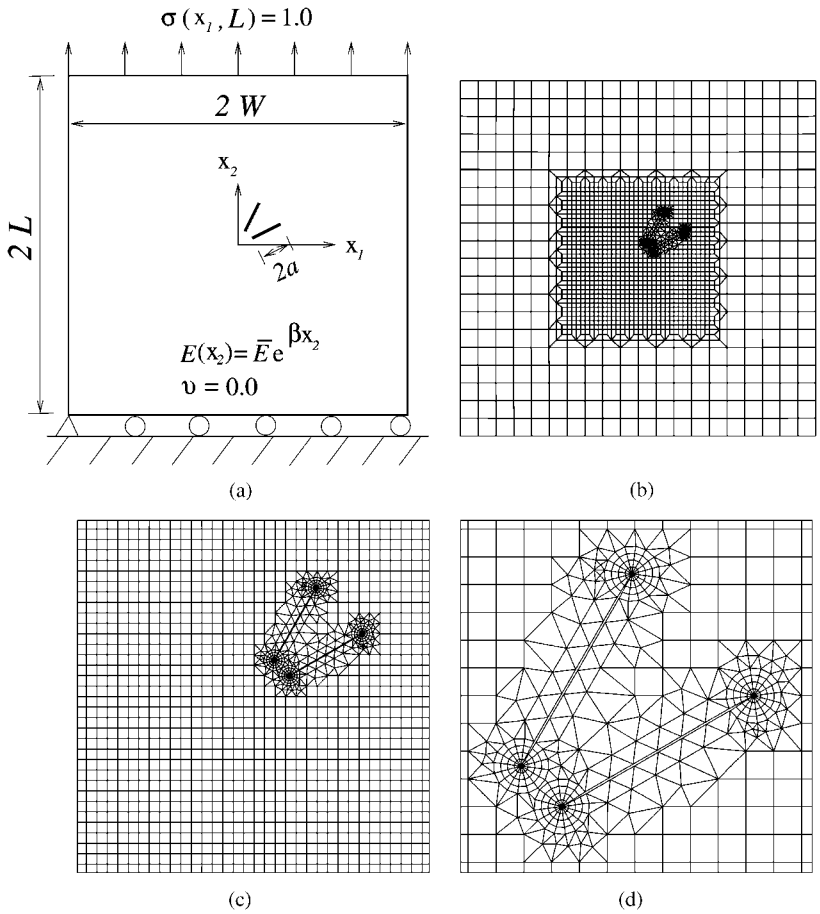

Figure 16. Two interacting cracks in a plate: (a) geometry and BCs; (b) finite element mesh; (c) mesh detail of centre region; (d) mesh detail around crack tips showing 16 sectors and four rings of elements around each tip.

8. CONCLUSIONS AND EXTENSIONS

This paper presents a general purpose FEM formulation and implementation for linearly elastic FGMs and for fracture of FGMs considering mixed-mode cracks. The displacement correlation technique (DCT), the modified crack closure (MCC) method and the J_k^*-integral are investigated in the context of fracture of FGMs. In the present investigation, carefully designed transition elements emanating from the crack tip region are used.

Extensive numerical results are presented, from which the following conclusions may be drawn. In general, the J_k^*-integral and the MCC method are superior to the DCT. For pure mode I problem, the J_k^*-integral and the MCC method provide almost the same results as the DCT. For mixed-mode problems, the MCC provides accurate SIFs independent of the choice of the characteristic length ($\delta_1 = \Delta a$) for the first ring of elements around the crack

tip. Within limits, the DCT provides better results as the characteristic length (δ_1) becomes smaller. The J_k^*-integral is sensitive to the choice of the characteristic length (δ_1) and it shows good performance for δ_1 in the range $a/24$ (test results were not shown for this case) to $a/18$.

This work has presented reliable methods to evaluate SIFs in FGMs. Thus it offers room for potential extension such as fracture analysis of orthotropic FGMs and mixed-mode crack initiation and propagation in FGMs. These topics are currently being pursued by the authors.

ACKNOWLEDGEMENTS

We gratefully acknowledge the support from the National Science Foundation (NSF) under grant No. CMS-9996378 (Mechanics and Materials Program). We also would like to thank Prof. R. H. Dodds (from the Department of Civil and Environmental Engineering at UIUC) for very useful comments and suggestions on this work.

REFERENCES

1. Hirano T, Teraki J, Yamada T. On the design of functionally gradient materials. In *Proceedings of the First International Symposium on Functionally Gradient Materials*. Yamanouchi M, Koizumi M, Hirai T, Shiota I (eds). Sendai, Japan, 1990; 5–10.
2. Koizumi M. The concept of FGM. In *Proceedings of the Second International Symposium on Functionally Gradient Materials Ceramic Transactions*, vol. 34. Holt JB, Koizumi M, Hirai T, Munir ZA (eds). The American Ceramic Society: Westerville, Ohio, 1993; 3–10.
3. Hirai T. Functionally gradient materials and nanocomposites. In *Proceedings of the Second International Symposium on Functionally Gradient Materials*, *Ceramic Transactions*, vol. 34. Holt JB, Koizumi M, Hirai T, Munir ZA (eds). The American Ceramic Society: Westerville, Ohio, 1993; 11–20.
4. Suresh S, Mortensen A. *Fundamentals of Functionally Graded Materials*. IOM Communications Ltd: London, 1998.
5. Igari T, Notomi A, Tsunoda H, Hida K, Kotoh T, Kunishima S. Material properties of functionally gradient material for fast breeder reactor. In *Proceedings of the First International Symposium on Functionally Gradient Materials*. Yamanouchi M, Koizumi M, Hirai T, Shiota I (eds). Sendai: Japan, 1990; 209–214.
6. Tani J, Liu GR. Surface waves in functionally gradient piezoelectric plates. *JSME International Journal Series A* (*Mechanics and Material Engineering*) 1993; **36**(2):152–155.
7. Hirano T, Whitlow LW, Miyajima M. Numerical analysis of efficiency improvement in functionally gradient thermoelectric materials. In *Proceedings of the Second International Symposium on Functionally Gradient Materials*, *Ceramic Transactions*, vol. 34. Holt JB, Koizumi M, Hirai T, Munir ZA (eds). The American Ceramic Society: Westerville, Ohio, 1993; 23–30.
8. Osaka T, Matsubara H, Homma T, Mitamura S, Noda K. Microstructural study of electroless-plated CoNiReP/NiMoP double-layered media for perpendicular magnetic recording. *Japanese Journal of Applied Physics* 1990; **29**(10):1939–1943.
9. Watanabe Y, Nakamura Y, Fukui Y, Nakanishi K. A magnetic-functionally graded material manufactured with deformation-induced martensitic transformation. *Journal of Materials Science Letters* 1993; **12**(5):326–328.
10. Koike Y. Graded-index and single mode polymer optical fibers. In *Electrical*, *Optical*, *and Magnetic Properties of Organic Solid State Materials*, vol. 247. Chiang LY, Garito AG, Sandman DJ (eds). Materials Research Society Proceedings: Pittsburgh, PA, 1992; 817.
11. Desplat JL. Recent development on oxygenated thermionic energy converter—Overview. *Proceedings of the Fourth International Symposium on Functionally Graded Materials*, Tsukuba City, Japan, 1996.
12. Watari F, Yokoyama A, Saso F, Uo M, Ohkawa S, Kawasaki T. EPMA elemental mapping of functionally graded dental implant in biocompatibility test. *Proceedings of the Fourth International Symposium on Functionally Graded Materials*, Tsukuba City, Japan, 1996.
13. Oonishi H, Noda T, Ito S, Kohda A, Yamamoto H, Tsuji E. Effect of hydroxyapatite coating on bone growth into porous Titanium alloy implants under loaded conditions. *Journal of Applied Biomaterials* 1994; **5**(1): 23–27.
14. Getto H, Ishihara S. Development of the fire retardant door with functional gradient wood. *Proceedings of the Fourth International Symposium on Functionally Graded Materials*, Tsukuba City, Japan, 1996.
15. Eischen JW. Fracture of non-homogeneous materials. *International Journal of Fracture* 1987; **34**:3–22.
16. Gu P, Dao M, Asaro RJ. A simplified method for calculating the crack-tip field of functionally graded materials using the domain integral. *ASME Journal of Applied Mechanics* 1999; **66**(1):101–108.

17. Anlas G, Santare MH, Lambros J. Numerical calculation of stress intensity factors in functionally graded materials. *International Journal of Fracture* 2000; **104**:131–143.
18. Marur PR, Tippur HV. Numerical analysis of crack-tip fields in functionally graded materials with a crack normal to the elastic gradient. *International Journal of Solids and Structures* 2000; **37**:5353–5370.
19. Bao G, Wang L. Multiple cracking in functionally graded ceramic/metal coatings. *International Journal of Solids and Structures* 1995; **32**(19):2853–2871.
20. Bao G, Cai H. Delamination cracking in functionally graded coating/metal substrate systems. *Acta Mechanica* 1997; **45**(3):1055–1066.
21. Lee YD, Erdogan F. Residual/thermal stresses in FGM and laminated thermal barrier coatings. *International Journal of Fracture* 1995; **69**:145–165.
22. Williams ML. On the stress distribution at the base of a stationary crack. *ASME Journal of Applied Mechanics* 1957; **24**:109–114.
23. Jin ZH, Noda N. Crack tip singular fields in non-homogeneous materials. *ASME Journal of Applied Mechanics* 1994; **61**(3):738–740.
24. Eftis J, Subramonian N, Liebowitz H. Crack border stress and displacement equations revisited. *Engineering Fracture Mechanics* 1977; **9**:189–210.
25. Gray LJ, Paulino GH. Crack tip interpolation revisited. *SIAM Journal on Applied Mathematics* 1998; **58**(2): 428–455.
26. Shih CF, de Lorenzi HG, German MD. Crack extension modeling with singular quadratic isoparametric elements. *International Journal of Fracture* 1976; **12**:647–651.
27. Rybicki EF, Kanninen MF. A finite element calculation of stress intensity factors by a modified crack closure integral. *Engineering Fracture Mechanics* 1977; **9**:931–938.
28. Irwin GR. Analysis of stresses and strains near the end of a crack traversing a plate. *ASME Journal of Applied Mechanics* 1957; **24**:354–361.
29. Jin ZH, Batra RC. Some basic fracture mechanics concepts in functionally graded materials. *Journal of the Mechanics and Physics of Solids* 1996; **44**:1221–1235.
30. Ramamurthy TS, Krishnamurthy T, Narayana KB, Vijayakumar K, Dataguru B. Modified crack closure integral method with quarter point elements. *Mechanics Research Communications* 1986; **13**(4):179–186.
31. Raju IS. Calculation of strain-energy release rates with high order and singular finite elements. *Engineering Fracture Mechanics* 1987; **28**(3):251–274.
32. Herrmann AG. On conservation laws of continuum mechanics. *International Journal of Solids and Structures* 1981; **17**:1–9.
33. Eischen JW. An improved method for computing the J_2 integral. *Engineering Fracture Mechanics* 1987; **26**(5):691–700.
34. Rice JR. Path-independent integral and the approximate analysis of strain concentration by notches and cracks. *ASME Journal of Applied Mechanics* 1968; **35**:379–386.
35. Raju IS, Shivakumar KN. An equivalent domain integral method in the two-dimensional analysis of mixed mode crack problems. *Engineering Fracture Mechanics* 1990; **37**(4):707–725.
36. Wawrzynek PA. Interactive finite element analysis of fracture processes: an integrated approach. *M.S. Thesis*, Cornell University, 1987.
37. Wawrzynek PA, Ingraffea AR. Discrete modeling of crack propagation: theoretical aspects and implementation issues in two and three dimensions. *Report 91-5*, School of Civil Engineering and Environmental Engineering, Cornell University, 1991.
38. Hughes TJR. *The Finite Element Method*: *Linear Static and Dynamic Finite Element Analysis*. Prentice-Hall: NJ, 1987.
39. Paulino GH, Kim JH. The weak patch test for nonhomogeneous materials modeled with graded finite elements (submitted for publication).
40. Erdogan F, Wu BH. The surface crack problem for a plate with functionally graded properties. *ASME Journal of Applied Mechanics* 1997; **64**:449–456.
41. Chen J, Wu L, Du S. A modified J integral for functionally graded materials. *Mechanics Research Communications* 2000; **27**(3):301–306.
42. Belytschko T, Lu YY, Gu L. Element-free Galerkin methods. *International Journal for Numerical Methods in Engineering* 1994; **37**:229–256.
43. Marur PR, Tippur HV. Evaluation of mechanical properties of functionally graded materials. *Journal of Testing and Evaluation* 1998; **26**:539–545.
44. Konda N, Erdogan F. The mixed mode crack problem in a non-homogeneous elastic medium. *Engineering Fracture Mechanics* 1994; **47**(4):533–545.
45. Shbeeb NI, Binienda WK, Kreider KL. Analysis of the driving forces for multiple cracks in an infinite non-homogeneous plate, Part I: theoretical analysis. *ASME Journal of Applied Mechanics* 1999; **66**:492–500.
46. Shbeeb NI, Binienda WK, Kreider KL. Analysis of the driving forces for multiple cracks in an infinite non-homogeneous plate, Part II: numerical solutions. *ASME Journal of Applied Mechanics* 1999; **66**:501–506.

